

1 **Constructing a 3-D radially anisotropic crustal velocity**
2 **model for Oklahoma using full waveform inversion**

3 **Shuo Zhang¹ and Hejun Zhu^{1,2}**

4 ¹Department of Geosciences, The University of Texas at Dallas

5 ²Department of Physics, The University of Texas at Dallas

6 **Key Points:**

- 7 • We use induced earthquakes and full waveform inversion to construct a 3-D ra-
8 dially anisotropic seismic velocity for the crust of Oklahoma.
- 9 • Spatial distributions of inverted velocity and radial anisotropy agree with geolog-
10 ical provinces and tectonic deformation in Oklahoma.
- 11 • Lateral velocity heterogeneities have strong impacts on earthquake location, es-
12 pecially for epicentral depths.

Abstract

Over the past decade, the seismicity rate in the state of Oklahoma has increased significantly, which has been linked to industrial operations, such as saltwater injection. Taking advantage of induced earthquakes and recently deployed seismometers, we construct a 3-D radially anisotropic seismic velocity model for the crust of Oklahoma by using full waveform inversion. To mitigate the well-known cycle-skipping problem, we use misfit functions based on phase and waveform differences in several frequency bands. Relative velocity perturbations in the inverted model allow us to delineate major geological provinces in Oklahoma, such as the Anadarko and Arkoma Basins, as well as the Cherokee Platform and Shelf. In addition, radial anisotropy in the inverted model reflects deformation within the crust of Oklahoma, which might correlate with sedimentary layers, micro-cracks/fractures, as well as the dominant orientation of anisotropic minerals. The crystalline basement beneath Oklahoma can be inferred from the new velocity model, which enables us to better classify induced seismicity in current earthquake catalogs. Furthermore, synthetic experiments suggest that the new velocity model enables us to better constrain earthquake location in Oklahoma, especially for determining their depths, which are important for investigating induced seismicity.

Plain Language Summary

Taking advantage of induced earthquakes and seismometers deployed in Oklahoma in the last decade, we construct a radially anisotropic seismic model for the crust beneath Oklahoma by using full waveform inversion. The data misfit is iteratively reduced by about 40%, and predicted seismograms associated from the new velocity model can fit observations very well. We can identify geological structures from the velocity model, such as low velocity anomalies associated with the Anadarko Basin, and fast anomalies relative to the Cherokee Platform. Positive radial anisotropy in the shallow crust might reflect layered structure of sedimentary, while the negative radial anisotropy with the middle crust may relate to preferred orientation of anisotropic minerals, such as plagioclase, mica and amphibole. Furthermore, synthetic tests are used to illustrate the impact of lateral variations of seismic velocity on earthquake locations, especially for epicentral depths. Therefore, this new 3-D model provides us an opportunity to improve current catalogs of earthquakes in Oklahoma, and improve our understanding about the triggering mechanism of induced earthquakes.

1 Introduction

Located in the middle of the North American Plate, the state of Oklahoma is dominated by east-west oriented tectonic stress for a long time and results in its widespread crustal deformation (Whitaker & Engelder, 2006; Almqvist & Mainprice, 2017; Lund Sneek & Zoback, 2020). Due to its comparatively stable tectonic condition, seismicity in this area remains relatively low for decades. However, since 2008, seismologists observed a significant increase in seismicity in the state of Oklahoma, which reached a peak level around 2016 and then gradually decreased to a normal level. To date, many studies have attributed these unexpected earthquakes as induced seismicity related to industry activities, such as saltwater injection (Ellsworth, 2013; Walsh & Zoback, 2015; X. Chen et al., 2018) and hydraulic fracturing (Holland, 2013a; Rubinstein & Mahani, 2015; Skoumal et al., 2018). During this time, the 2011 Mw 5.7 Prague earthquake (Keranen et al., 2013; Sumy et al., 2014) and the 2016 Mw 5.8 Pawnee earthquake (Barbour et al., 2017; Pennington & Chen, 2017) are the two largest earthquakes ever occurred in Oklahoma, resulting in severe damage to the local community and infrastructure. In order to monitor these unusual seismic activities, many seismometers have been deployed in Oklahoma (Walter et al., 2020), giving us an opportunity to use seismic tomography to study the crustal structure of Oklahoma.

An accurate 3-D crustal velocity model is important for earthquake source estimations. With 1-D seismic velocity profiles and dense arrays in Oklahoma, several earthquake catalogs have been developed (Schoenball & Ellsworth, 2017; Cramer et al., 2017; Mueller, 2019), which enable us to delineate some previously unmapped 3-D fault systems in Oklahoma (Holland, 2013b; McNamara et al., 2015; Schoenball & Ellsworth, 2017). However, there are still a lot of randomly distributed earthquakes in these catalogs that cannot be directly linked to any fault systems. A number of studies have illustrated the impacts of lateral crustal velocity heterogeneities on earthquake location (Thurber, 1983; Michelini & Lomax, 2004; Font et al., 2013; Zhu, 2018), as well as moment tensor solutions (Q. Liu et al., 2004; X. Wang & Zhan, 2020; Takemura et al., 2021). Both of them are critical for studying earthquake triggering processes and delineating fault geometry in the subsurface. To date, there are few community-shared 3-D crustal velocity models in Oklahoma that can be used to potentially improve the accuracy of current earthquake catalogs and better delineate fault geometry (Tan et al., 2021).

77 Seismic tomography is a classical method to construct velocity models from seis-
78 mic data recorded at the Earth’s surface. The idea of iteratively constraining seismic model
79 parameters by minimizing mismatches between observations and predictions has been
80 proposed for a long time (Lailly & Bednar, 1983; Tarantola, 1984). Tromp et al. (2005)
81 recognized the generality of using the adjoint-state method in seismic tomography, which
82 combines high-quality seismic recordings with numerical modeling to map the spatial dis-
83 tribution of seismic parameters. So far, full waveform inversion (FWI) has been widely
84 utilized to constrain crustal and upper mantle structures in California (Tape et al., 2010;
85 K. Wang et al., 2020), Alaska (G. Chen et al., 2023), Austrilia (Fichtner et al., 2009),
86 New Zealand (Chow et al., 2020), Europe (Fichtner et al., 2013; Zhu et al., 2015), East-
87 ern Asia (M. Chen et al., 2017; Tao et al., 2018; Zhang et al., 2018), North America (Zhu
88 et al., 2017), Antarctic (A. Lloyd et al., 2020), North Atlantic (Rickers et al., 2013), and
89 the entire Earth (French & Romanowicz, 2014; Lei et al., 2020), etc.

90 In order to better investigate induced seismicity in Oklahoma, we construct a 3-
91 D seismic velocity model for the crust of Oklahoma by fully exploiting three-component
92 seismograms collected over the past several years. The lateral variations of seismic ve-
93 locity and radial anisotropy in the inverted model can be used to investigate geological
94 structures and deformation in Oklahoma (Fouch & Rondenay, 2006; J. Wang & Zhao,
95 2009; Long, 2013). In this paper, we first briefly review the tectonic evolution of the crust
96 beneath Oklahoma in section 2. The datasets and the initial model used in the inver-
97 sion are introduced in section 3. Section 4 presents determinations of misfit functions,
98 model parameterizations, and kernel processing. We illustrate the improvements in both
99 data and model domains in section 5. Section 6 discusses the reliability of the inverted
100 model, potential origins of radial anisotropy, depths of the crystalline basement, and im-
101 pact of velocity heterogeneities on earthquake locations.

102 **2 Brief Introduction of Tectonic Evolution in Oklahoma**

103 Oklahoma has experienced a long tectonic evolution history over the past 1.4 bil-
104 lion years, which forms its present-day crustal and lithospheric structure (Johnson & Luza,
105 2008). Since the Precambrian period, geological structures beneath Oklahoma experi-
106 enced numerous cycles of continental collision and rifting (Johnson & Luza, 2008). The
107 oldest rocks found in Oklahoma are Precambrian igneous and metamorphic rocks that
108 formed about 1.4 billion years ago (Sloss, 1988). Before being covered by shallow sea-

109 water in the early Paleozoic, the surface of Oklahoma was exposed and partly eroded (Hamilton,
110 1956). Due to the circulations of deposition and erosion during Silurian and Devonian (Chenoweth,
111 1968), multiple thin layers of black shale overlay on limestone and dolomite. Thick sed-
112 imentary layers were formed after rapid subsidence in the Carboniferous period (Johnson
113 & Luza, 2008), with most petroleum reservoirs found in Pennsylvanian shale in Okla-
114 homa (Ball et al., 1991). Most of Oklahoma was above sea level by the Triassic and Juras-
115 sic periods, which was then overlapped by the Cretaceous Sea. The weathered and loose
116 surface of Oklahoma, which was contributed by shale, sandstone, and limestone, were
117 characterized as the Quaternary sedimentary.

118 To date, the principal mountain belts, including the Ouachita, the Arbuckle, and
119 the Wichita mountains are located around the Southern Oklahoma Aulacogen, while
120 the Anadarko, the Arkoma, the Ardmore, and the Ouachita basins received sediments
121 with 2 to 12 km thickness (Johnson, 1996) (Figure 1A). The Anadarko basin is one of
122 the major tectonic provinces in Oklahoma (Evans, 1979), with sedimentary rocks rang-
123 ing from the Cambrian to the Permian periods. The thickest sedimentary column, in
124 excess of 12 km, is detected at the southern edge of the Anadarko basin, with the av-
125 erage thickness of the basin around 4.6 km (Kolawole et al., 2020). In contrast, the sed-
126 imentary thickness goes down to 0.6 km on the northern and western flanks of the basin, as
127 well as the Cherokee shelf and platform (Mitchell & Landisman, 1970). To date, the Anadarko
128 Basin is one of the largest oil production zones in America (Higley et al., 2014).

129 **3 Databases and The Initial Model**

130 **3.1 Distributions of Earthquakes and Seismometers**

131 We collect centroid moment tensor (CMT) solutions for earthquakes that occurred
132 between 2010 and 2018 (Figure 1D) from the Earthquake Center of St. Louis Univer-
133 sity (SLU; <https://www.eas.slu.edu/eqc/eqc.html>). These CMT solutions are jointly
134 inverted by using surface-wave spectrum amplitudes, radiation patterns, waveforms, and
135 first motions (Herrmann, 2013). In total, 153 earthquakes from the SLU catalog are used
136 in this study (Figure 1B), most of which are distributed around the Nemaha and Wilzetta
137 strike-slip fault zones with depths around 5 km (Figure 1E). They are small- to moderate-
138 sized earthquakes with magnitudes ranging from 3.4 to 4.8 (Figure 1F).

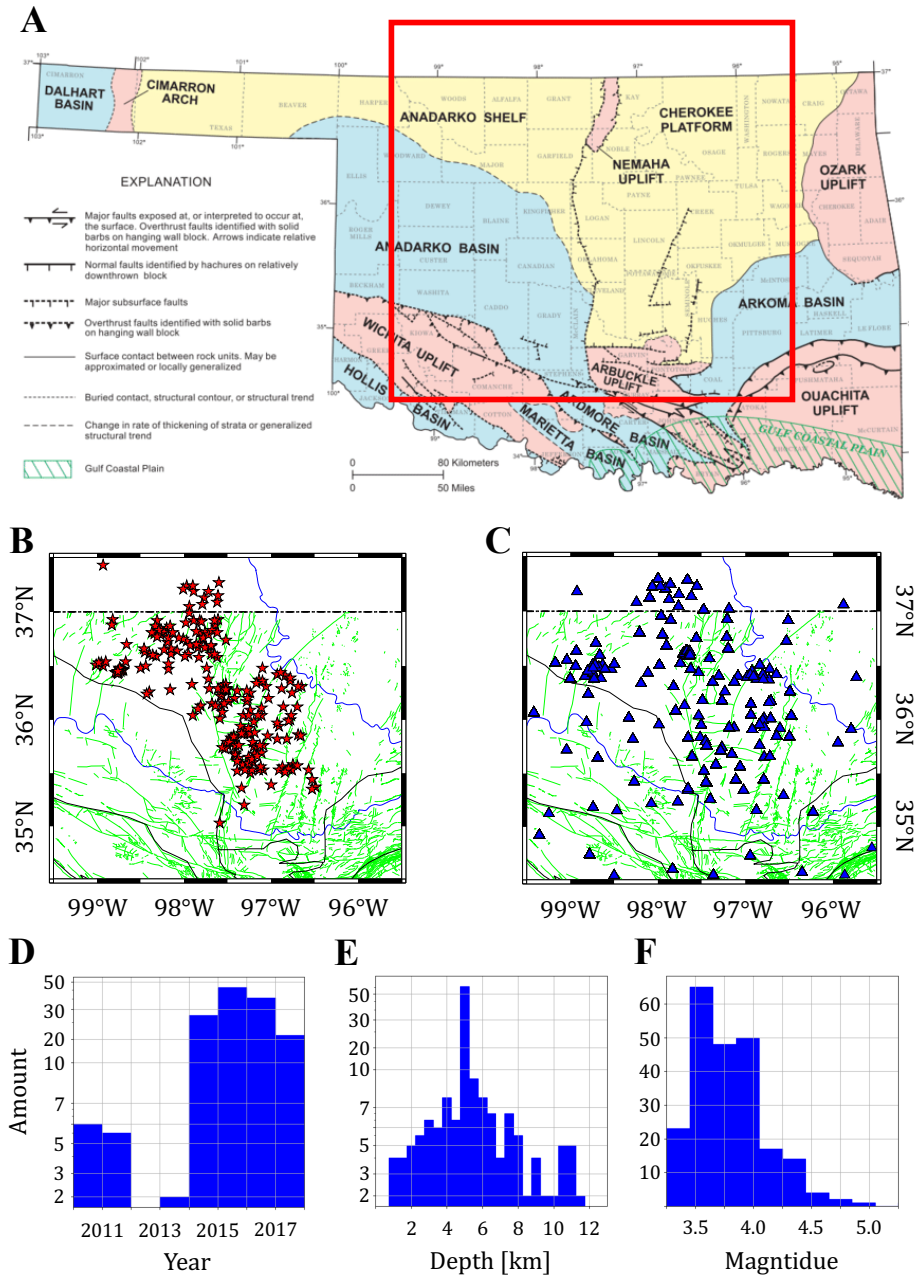


Figure 1. Tectonic map and distributions of earthquakes and stations used in this study. Panel A shows the simplified geological map modified from Northcutt and Campbell (1996). The red box represents the inversion region in this study. Panels B and C demonstrate the locations of 153 earthquakes (red stars) and 176 available stations (blue triangles). Green lines in panels B and C represent fault traces mapped at the Earth’s surface (Marsh & Holland, 2016), while thin black lines delineate geological provinces shown in panel A. Panels D to F show the histograms of occurring times, depths and magnitudes of collected earthquakes from the SLU catalog.

139 Three-component waveform recordings for these events are downloaded from the
 140 Data Management Center of the Incorporated Research Institutions of Seismology (IRIS-
 141 DMC). The USArray Transportable Array (TA) covered the study region from 2010 to
 142 2012, after which a number of temporary arrays have been deployed to monitor the in-
 143 creasing seismicity in Oklahoma. In total, 176 seismographic stations are used in this
 144 study (Figure 1C), allowing us to achieve a dense ray sampling for the state of Oklahoma.

145 **3.2 The Initial Model and Spectral Element Mesh**

146 We use a 3-D isotropic velocity model as the initial model, which was constructed
 147 by using adjoint tomography to fit vertical-vertical component ambient noise cross-correlation
 148 functions with a 5-40 s frequency band (Zhu, 2018). It gives us good fits for long-period
 149 surface waves with relatively low spatial resolutions, but does not include shallow sed-
 150 imentary layers due to the limited frequency bands. Here, we incorporate a shallow layer
 151 (<1.5 km) from Shen and Ritzwoller (2016) into the starting model in order to repre-
 152 sent sediments with slow seismic velocities in Oklahoma. The interface of these two mod-
 153 els (at 1.5 km depth) is smoothed by a Gaussian filter with standard deviation $\sigma = 200$ m,
 154 in order to avoid any artificial reflections. The simulation domain includes central and
 155 northern Oklahoma, as well as southern parts of Kansas, ranging from $34.5^\circ N$ to $37.5^\circ N$
 156 in latitude and $99.5^\circ W$ to $95.5^\circ W$ in longitude. The Moho depths of the study region
 157 vary from 38 to 44 km (Keller, 2013), thus, our model is truncated at 50 km depth. The
 158 Earth's surface is comparatively flat in Oklahoma, ranging from 200 to 600 m (Amante
 159 & Eakins, 2009).

160 SPECFEM3D_Cartesian is used to calculate forward and adjoint wavefields with
 161 the spectral element method (Komatitsch & Tromp, 1999; Peter et al., 2011). Topog-
 162 raphy from ETOPO1 (Amante & Eakins, 2009) is incorporated into the discretized spectral-
 163 element mesh. The entire mesh includes 428,544 spectral elements and 28,340,784 Gauss-
 164 Lobatto-Legendre grid points. The minimum resolvable period is around 1.61 s and the
 165 minimum element size is approximately 1.25 km at the Earth's surface. With 128 cores
 166 on the Lonestar 6 cluster at the Texas Advanced Computing Center (TACC), it takes
 167 48 minutes to perform one forward simulation and approximately 2 hours for calculat-
 168 ing misfit gradients for each individual event.

169 4 Method

170 4.1 Choices of Misfit Functions

171 The specific misfit function in FWI determines the purposes and eventual perfor-
 172 mance of the inversion (Tromp et al., 2005). In the last decades, a variety of misfit func-
 173 tions have been designed based on travel-times differences (Luo & Schuster, 1991), sur-
 174 face wave dispersion curves (Beatty et al., 2002; Dal Moro et al., 2007), envelopes differ-
 175 ences (Bozdağ et al., 2011; Wu et al., 2014), dynamic wrapping functions (Ma & Hale,
 176 2013), adaptive matching filters (Warner & Guasch, 2016; Zhu & Fomel, 2016), cross-
 177 correlation functions (Y. Liu et al., 2017; Tao et al., 2017), Wasserstein distances (Métivier
 178 et al., 2016; Yang & Engquist, 2018), etc. Among them, the L2 norm of waveform dif-
 179 ferences is the classical misfit to constrain seismic velocity models. However, it suffers
 180 from nonlinearity and cycle-skipping problems (Virieux & Operto, 2009). In order to mit-
 181 igate these difficulties, two misfit functions based on phase and waveform differences are
 182 used in this study. Here, FLEXWIN is applied to automatically select useful windows,
 183 which allows us to compare phase shifts, STA/LTA, as well as envelopes of observed and
 184 predicted waveforms (Maggi et al., 2009).

185 We first update the velocity models by reducing phase differences. Here, frequency-
 186 dependent phase differences are measured by using a multi-taper technique (Tape et al.,
 187 2010),

$$\chi_1 = \frac{1}{2} \sum_s \sum_r \sum_m N_m \int \left[\frac{\Delta\tau_m(\omega)}{\sigma_m(\omega)} \right]^2 d\omega \quad , \quad (1)$$

188 where $\Delta\tau_m$ denotes the phase difference between observations and predictions for m com-
 189 ponent, and σ_m is the associated uncertainty of the phase measurement. ω is the angu-
 190 lar frequency, N_m denotes the weighting factor to balance the contributions of different
 191 components. The total misfit (Equation 1) is the summation over all earthquakes s , sta-
 192 tions r , and wave components m . To further mitigate the nonlinearity of FWI, a multi-
 193 scale strategy (Bunks et al., 1995) is applied via inverting the velocity model using three
 194 different frequency bands, 10-30 s, 5-30 s, and 2-30 s, sequentially.

195 Once the travel-time differences between observed and predicted waveforms are less
 196 than half period of the dominate frequency, we switch to the L2 waveform misfit as,

$$\chi_2 = \frac{1}{2} \int [\hat{d}(t) - \hat{s}(t)]^2 dt \quad , \quad (2)$$

197 where $\hat{d}(t)$ and $\hat{s}(t)$ denote the normalized observations and predictions, in order to mit-
 198 igate potential errors for moment magnitude from CMT solutions. This second waveform-
 199 based misfit enables us to further improve the spatial resolution of the inversion.

200 4.2 Model Parameterization

201 Radial anisotropy, with five independent elastic constants (C_{11} , C_{13} , C_{33} , C_{44} , C_{66}),
 202 is introduced in the model update to solve the Rayleigh-Love discrepancy (Anderson,
 203 1961; Harkrider, 1964; Debayle & Kennett, 2000). Since the phase measurements are more
 204 sensitive to wavespeeds, we use the following five model parameters,

$$\begin{aligned} \alpha_h &= \sqrt{\frac{C_{11}}{\rho}} \quad , \\ \alpha_v &= \sqrt{\frac{C_{33}}{\rho}} \quad , \\ \beta_h &= \sqrt{\frac{C_{66}}{\rho}} \quad , \\ \beta_v &= \sqrt{\frac{C_{44}}{\rho}} \quad , \\ \eta &= \frac{C_{13}}{C_{11} - 2C_{44}} \quad . \end{aligned} \quad (3)$$

205 where ρ stands for the density. α_h and α_v are the velocities of horizontally and verti-
 206 cally polarized P-wave. β_h and β_v are the velocities of horizontally and vertically polar-
 207 ized S-wave. η is the radial anisotropy parameter.

208 The mass density ρ is approximated by the following empirical relationship,

$$\delta \ln \rho = 0.33 \ln \beta \quad , \quad (4)$$

209 where the Voigt average of isotropic compressional- and shear-wave velocities, α and β ,
 210 can be computed as

$$\alpha = \sqrt{\frac{2\alpha_h^2 + \alpha_v^2}{3}} \quad ,$$

$$\beta = \sqrt{\frac{2\beta_h^2 + \beta_v^2}{3}} . \quad (5)$$

211 We define the radial anisotropy (RA) as,

$$RA = \frac{\beta_h - \beta_v}{\beta} , \quad (6)$$

212 For each iteration, four model parameters, α_h , α_v , β_h , and β_v , are updated simul-
 213 taneously. Thus, the misfit perturbation can be expressed as a volumetric integral over
 214 relative perturbations of these four model parameters as

$$\delta\chi = \int_V K_{\alpha_h} \delta\ln\alpha_h + K_{\alpha_v} \delta\ln\alpha_v + K_{\beta_h} \delta\ln\beta_h + K_{\beta_v} \delta\ln\beta_v dV , \quad (7)$$

215 where K_{α_h} , K_{α_v} , K_{β_h} and K_{β_v} are the misfit gradients with respect to four radially anisotropic
 216 elastic model parameters.

217 We use the approximated inverse of the diagonal Hessian as the pre-conditioner to
 218 balance amplitudes at shallow and deeper depths, and mitigate singular values at source
 219 and receiver locations (Luo, 2012; Luo et al., 2015),

$$P(\mathbf{x}) = \frac{1}{\int \partial^2 \mathbf{s}(\mathbf{x}, t) \cdot \partial^2 \mathbf{s}^\dagger(\mathbf{x}, T - t) dt} , \quad (8)$$

220 where \mathbf{s} and \mathbf{s}^\dagger denote the forward and adjoint displacement wavefields, respectively.

221 We also employ a 3-D Gaussian function to smooth the preconditioned kernels. Its
 222 standard deviation varies with the dominant wavelength of the inversion. A conjugate-
 223 gradient method is utilized to update the model parameters (Fletcher & Reeves, 1964;
 224 Matthies & Strang, 1979), with the step length determined by a quadratic interpolation (Tape
 225 et al., 2007).

226 5 Results

227 5.1 Waveform Fitting

228 Taking one earthquake occurred in November 8th 2015 as an example (Figure 2A),
 229 we compare observed and predicted seismograms to demonstrate the performance of the
 230 inversion. The locations and azimuthal distributions of recorded seismometers are shown

231 in Figures 2A and C. Compared with results from the initial model (Figures 3A and S1
 232 in Supporting Information), simulations from the new model fit observed waveforms much
 233 better. For instance, for short epicentral distances, predictions can perfectly match ob-
 234 servations, while there are still some residuals for longer epicentral distances. Other than
 235 fundamental mode surface waves, the inverted model can also reproduce higher-mode
 236 oscillations, which can be clearly observed in 5-30 s and 2-30 s frequency bands (Figures 2B
 237 and S2 in Supporting Information). For further comparisons, we also simulate wave prop-
 238 agation with the same earthquake and corresponding stations by using a 1-D velocity
 239 profile (OGS-1D) provided by the Oklahoma Geological Survey (Darold et al., 2015). For
 240 short epicentral distances, the OGS-1D model provides comparably good fittings with
 241 observed data, however, it fails to fit observations with long epicentral distances (Fig-
 242 ures 3C and S3 in Supporting Information). More details on waveform comparisons with
 243 different velocity models can be found in Section S1 of Supporting Information.

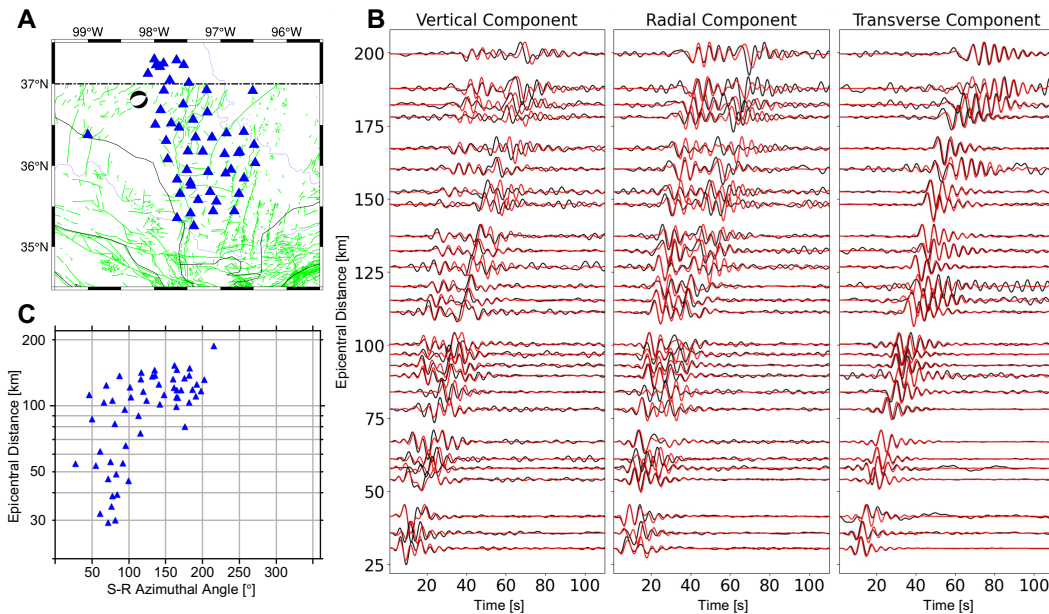


Figure 2. Comparison between observed (black) and predicted (red) waveforms based on the inverted model. The particular earthquake (beachball) and corresponding seismometers (triangle) are shown in panel A. Comparisons of vertical, radial, and transverse component seismograms (with 5-30 s passband) are shown from left to right in panel B. Panel C illustrates the distributions of azimuthal angles and epicentral distances for selected seismograms.

244 Beyond this particular event, we also present the evolution of data residuals in Fig-
 245 ure 4A. In order to mitigate the cycling-skipping problem, three frequency bands, 10-
 246 30 s, 5-30 s, 2-30 s, are applied sequentially, with the same phase-based misfit (Equa-
 247 tion 1). It is then followed by another five iterations with the L2 norm waveform-based
 248 misfit (Equation 2) in 5-30 s frequency band. Because of different frequency bands and
 249 misfits, these four stages are not directly comparable. Therefore, we normalize the data
 250 misfit within each individual stage for a better comparison. When using the phase-based
 251 misfit in 10-30 s (Figure 4A), the data misfit is reduced by about 30% for each individ-
 252 ual component. While for higher frequency bands (5-30 s and 2-30 s), the phase differ-
 253 ence of the transverse component decreases much faster than the other two components.
 254 The data misfit is reduced by around 25% after using the phase-based misfit. In contrast,
 255 after switching to the L2 norm waveform misfit in the last five iterations, we observe a
 256 larger misfit reduction for vertical and radial components (22%) than the transverse com-
 257 ponent (13%).

258 The robustness of the inversion in the data domain can be further illustrated by
 259 comparing the histograms of time shifts between the initial and inverted models (Fig-
 260 ures 4B-D). The isotropic initial velocity model (Zhu, 2018) still produces 0.5-1.0 s mean
 261 travel time errors for three components in the frequency band of 2-30 s. The inverted
 262 model enables us to reduce the averaged travel-time error to less than 0.2 s. For instance,
 263 the mean travelttime error for the vertical component is reduced from 1.09 s to 0.19 s.
 264 In addition, FLEXWIN can detect more windows for the inverted model than the ini-
 265 tial model, because of the improvement of overall waveform match. For instance, the to-
 266 tal number of detected time windows for the radial component is increased from 1,140
 267 to 2,099 after the inversion.

268 5.2 3-D Isotropic Shear Wave Velocity Model

269 We first compute the 1-D velocity profile (FWI-1D) by averaging lateral hetero-
 270 geneities of the inverted 3-D model, and compare it with OGS-1D in Figure 5A. Start-
 271 ing from slow sedimentary layers with $V_p = 3.0 \text{ km/s}$ and $V_s = 1.7 \text{ km/s}$, both FWI-
 272 1D and OGS-1D consistently increase with depths. Large discrepancies exist between
 273 2 to 7 km, with FWI-1D being slower than OGS-1D by about 9% in P-wave velocity and
 274 3% in S-wave velocity. Considering better waveform comparisons as shown in Figures 3B
 275 and C, this comparatively slow velocity at depths of 4-7 km in FWI-1D (Figure 5A) is

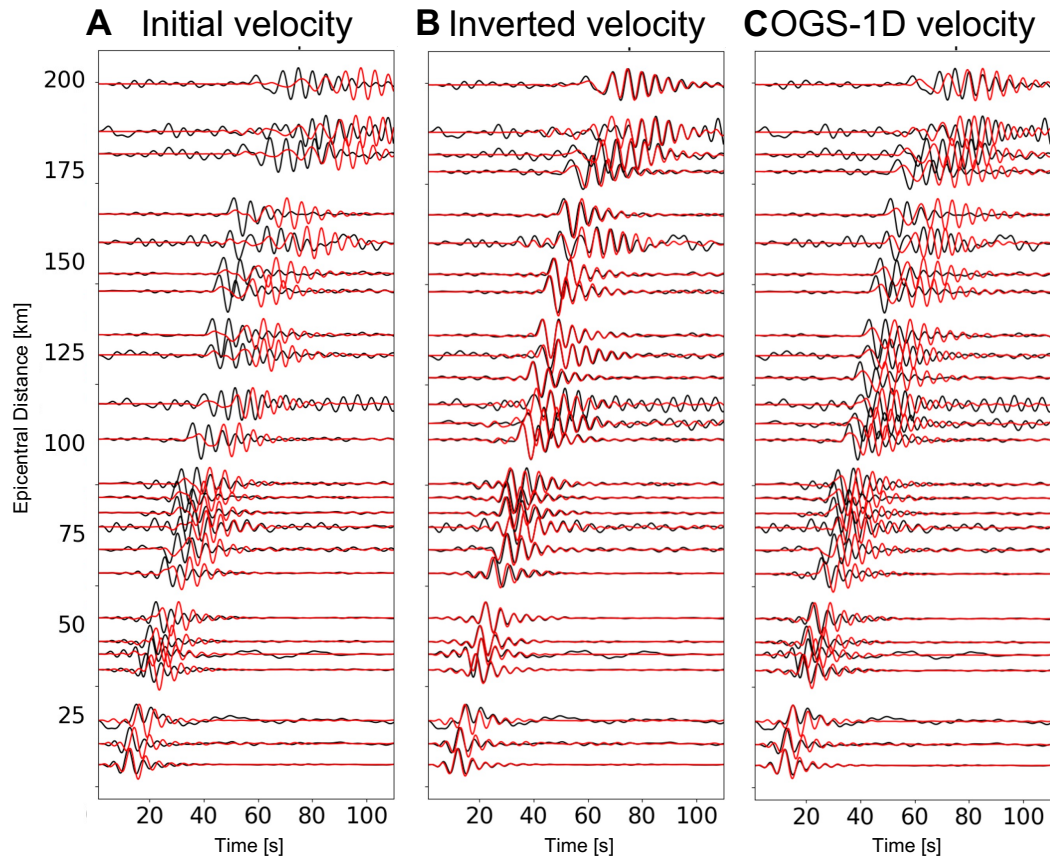


Figure 3. Comparison between transverse component observed (black) and predicted (red) seismograms from different velocity models. Locations of the earthquake and corresponding seismometers are shown in Figure 2A. Panels A to C are resulted from the initial model, inverted model, and OGS-1D profile (Darold et al., 2015), respectively. All seismograms are filtered with 5-30 s passband.

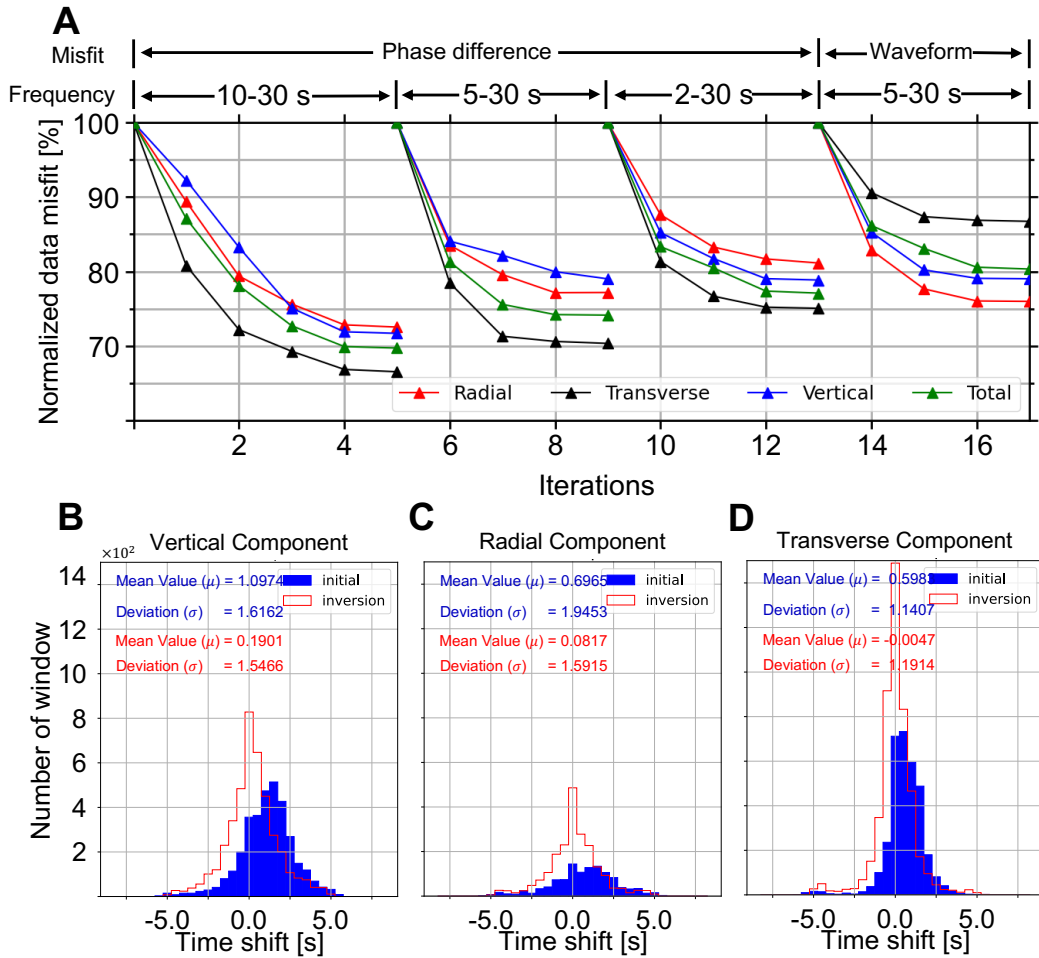


Figure 4. Comparisons of data residuals and travel time histograms. Panel A shows the evolution of data residuals with four stages of total 17 iterations, with different frequency bands and misfit functions. The data misfits are normalized within each individual stage for better comparison. Panels B-D compare the histograms of travel-time differences between three components, observed and predicted seismograms from the initial (blue) and inverted (red) velocity models.

276 required for waveform fitting. These two 1D velocity profiles are basically consistent with
 277 each other in the middle crust. Because of limited frequencies and ray-path coverage,
 278 our inversion is not sensitive to velocity perturbations at depths greater than 30 km.

279 We also compute relative velocity perturbations (Figures 5B-E), with respect to
 280 FWI-1D by using $V_{rel} = \ln \frac{V_{3D}}{V_{1D}}$. Two major features can be observed within the up-
 281 permost crust (Figure 5B), with slow anomalies for basin areas and fast anomalies for
 282 the Cherokee Shelf and Platform. In vertical profiles, the depths of the fast anomaly change
 283 from 10 km in the Cherokee Shelf (Figures 6G and I) to less than 5 km in the Chero-
 284 kee Platform (Figure 6G), which basically agree with geological survey results (Northcutt
 285 & Campbell, 1996; Johnson & Luza, 2008; Xu et al., 2009).

286 In contrast to the fast Cherokee Shelf and Platform, the Anadarko and Arkoma
 287 Basins are fulfilled with sandstone and shale after frequent erosion and deposit (Johnson
 288 & Luza, 2008), where seismic velocity perturbations are imaged as slow as -10%. In ad-
 289 dition, porous and layered structures in these sedimentary basins might further slow down
 290 the apparent velocity due to attenuation and scattering effects (Houtz & Ludwig, 1979;
 291 Sams et al., 1997; Yu et al., 2015). The NE-SW distribution of the slow velocity anomaly
 292 is consistent with the geological boundaries of the Anadarko Basin (Perry, 1989). Sim-
 293 ilar observations can also be obtained for the Arkoma Basin. The wedge shape of the
 294 slow velocity anomaly in the Anadarko Basin, with the lower bound at about 15 km (Fig-
 295 ure 6H and I), is consistent with geological investigations (Perry, 1989; Ball et al., 1991;
 296 Northcutt & Campbell, 1996). Another fast velocity anomaly can be observed in the mid-
 297 dle crust beneath slow basins in Figure 6H, which might be related to the Arbuckle Up-
 298 lift (Johnson & Luza, 2008) in south Oklahoma.

299 5.3 Radial Anisotropy

300 The magnitude of RA, defined by Equation 6, ranges from -5% to +5% in our in-
 301 verted model. Two large RA anomalies are imaged, a large negative anomaly within the
 302 middle crust is overlain by a positive anomaly in the uppermost crust (Figures 5J-L).
 303 The positive perturbation is located around the Nemaha-Wilzetta Fault System, which
 304 connects the Cherokee Shelf in the west and the Cherokee Platform in the east (Figure 5F).
 305 In spite of its large amplitude (+5%), this positive RA is comparatively thin. Underneath

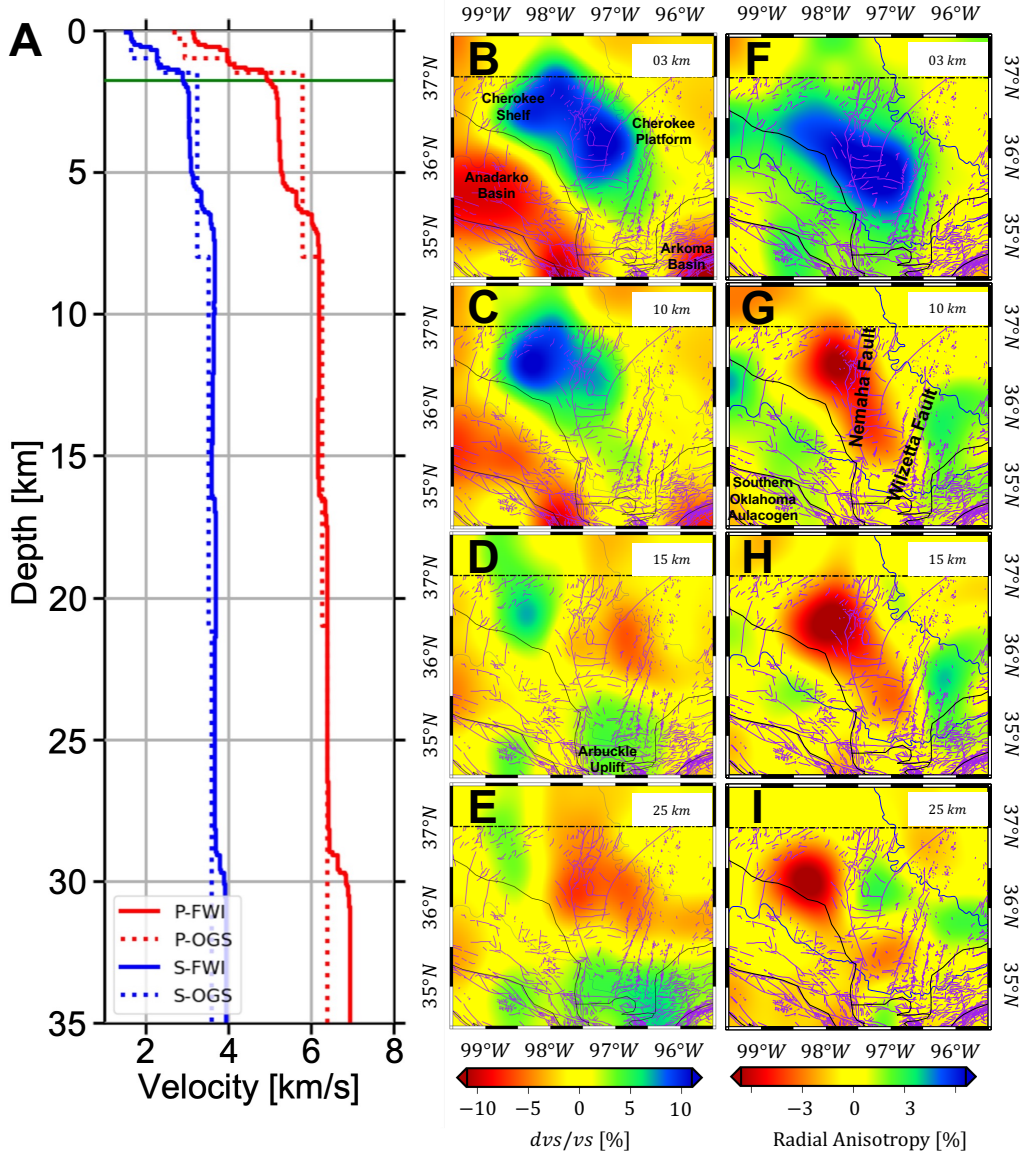


Figure 5. Vertical and horizontal variations of seismic velocities within the inverted model. Panel A compares absolute P (red) and S (blue) wave velocities from OGS-1D (dashed) and FWI-1D (solid) profiles. Panels B to E show relative S velocity variations at depths of 3, 10, 15 and 25 km. Corresponding radial anisotropy at these depths are shown in panels F to I.

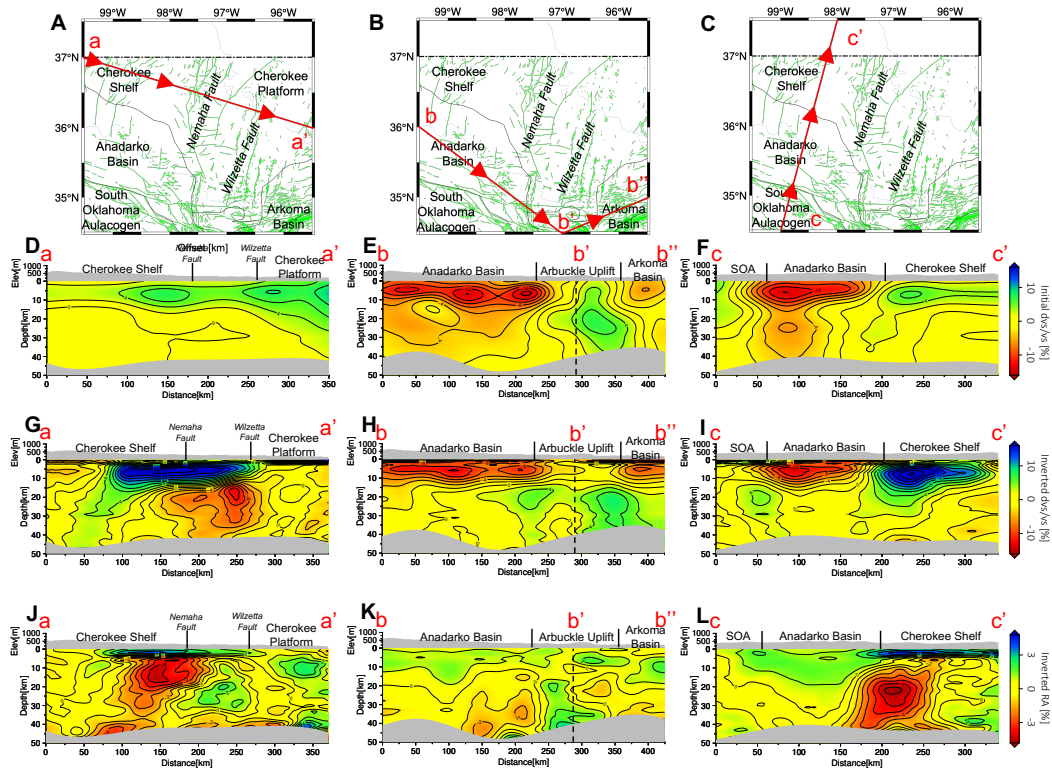


Figure 6. Vertical cross sections of the initial and inverted models and their radial anisotropy. Panels D, G and J are extracted from line a-a' in panel A. Panels E, H and K are extracted from line b-b'-b'' in panel B, where the dashed lines indicate the turning point b'. Panels F, I and L are extracted from line c-c' in panel C. Panels D, E and F illustrate shear wave velocity perturbations from the initial velocity model. Panels G, H and I show relative shear wave velocity perturbations from the inverted velocity model. Panels J, K and L are radial anisotropy in the inverted model.

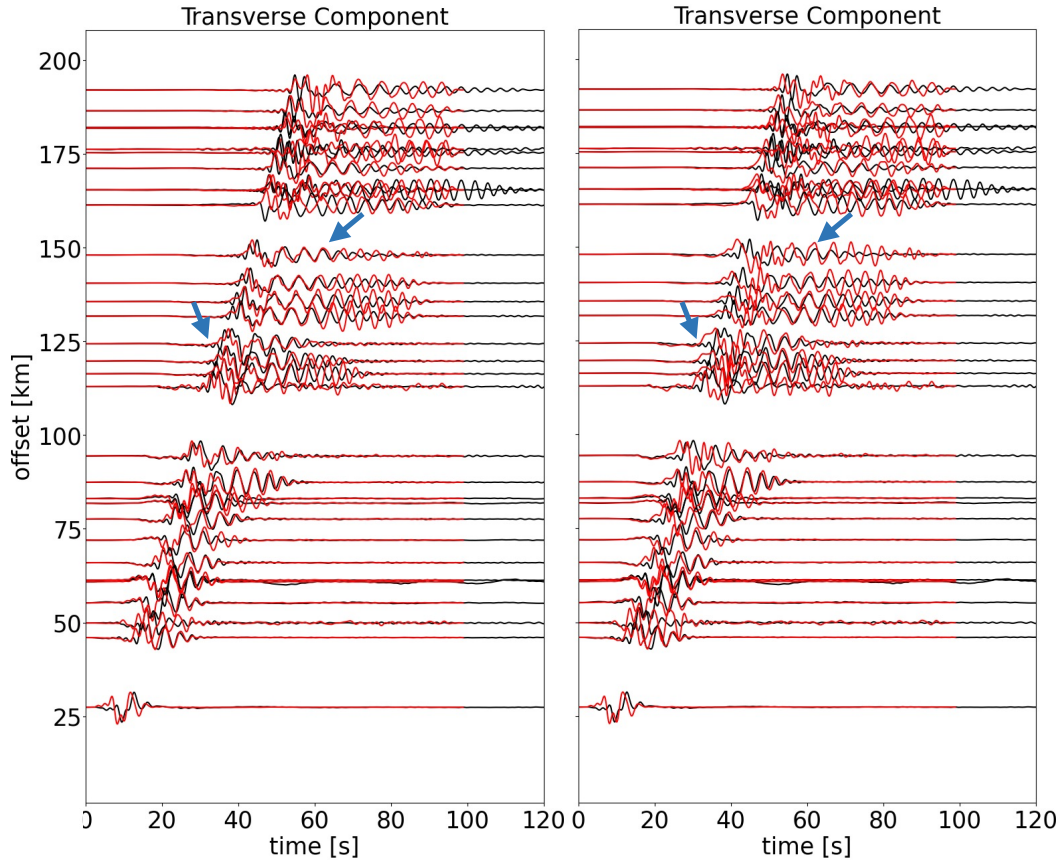


Figure 7. Necessity of incorporating radial anisotropy in the inverted model. Red traces are predicted seismograms based on the inverted model (left) and the modified velocity model after removing positive RA in the uppermost crust (right), while black traces are observations. Only transverse component seismograms are shown here. The locations of earthquake and corresponding stations are the same as Figure 2A. All seismograms are filtered with a 2-30 s passband.

306 the Anadarko Basin, the weak positive RA (less than +3%) goes down to depths around
 307 20 km (Figures 6K and L).

308 In contrast to the uppermost crust, a negative RA perturbation (-5%) is imaged
 309 within the middle/lower crust beneath the Nemaha-Wilzetta Fault Zone, which is sur-
 310 rounded by relatively weak positive anomalies (+3%) beneath the Anadarko Basin and
 311 Cherokee Platform (Figures 5G and H). As the depth increases, the center of this neg-
 312 ative anomaly moves northward to the Cherokee Shelf (Figure 5I). The origin of these
 313 RA anomalies will be discussed in section 6.2.

314 To further evaluate the necessity of including radial anisotropy in our inversion,
 315 we build another 3-D velocity model by removing the positive RA within the uppermost
 316 crust. A Gaussian filter with $\sigma = 0.2 \text{ km}$ is applied to remove artificial contrasts due
 317 to this modification. All waveforms are filtered with a 2-30 s passband. Compared with
 318 the original inverted model (Figure 7A), seismograms from the modified velocity model (Fig-
 319 ure 7B) produce much larger mismatches in both travel-times and amplitudes. This com-
 320 parison demonstrates the necessity of incorporating radial anisotropy in the inversion.

321 6 Discussion

322 6.1 Assessments of the Inverted Model

323 A checkerboard model with a standard deviation $\sigma_h = 30 \text{ km}$ in the horizontal
 324 direction and $\sigma_v = 10 \text{ km}$ in the vertical direction is used to analyze the resolution of
 325 our inversion. The amplitude of this checkerboard model is limited within $\pm 15\%$ with
 326 respect to the maximum of the inverted model. The action of the Hessian on each model
 327 parameter can be approximated by the subtraction of gradients based on perturbed and
 328 original 3-D velocity models. In order to evaluate cross-talks among four model param-
 329 eters, we perturb one model parameter at each time and leave the other three model pa-
 330 rameters unchanged.

331 For instance, Figure 8 illustrates the approximated Hessian action when perturb-
 332 ing β_v alone. Regardless of the imperfect shapes resulting from the uneven distribution
 333 of seismometers and earthquakes, we are able to successfully recover the positive and neg-
 334 ative Gaussian anomalies in the checkerboard model (Figures 8E and e). In addition, the
 335 amplitude of the recovered perturbations in β_v is ten times larger than the other three
 336 model parameters. These results suggest that the inversion is less contaminated by the
 337 tradeoff among different model parameters. The other three experiments by perturbing
 338 α_h , α_v , and β_h are shown in Section S2 of Supporting Information, which basically give
 339 us similar conclusions.

340 6.2 Origin of Radial Anisotropy

341 Radial anisotropy can be used as an indicator for investigating tectonic deforma-
 342 tion and dynamic processes of the crust (Fouch & Rondenay, 2006; J. Wang & Zhao, 2009;
 343 Long, 2013). Major origins of seismic anisotropy include lattice-preferred orientation (LPO)

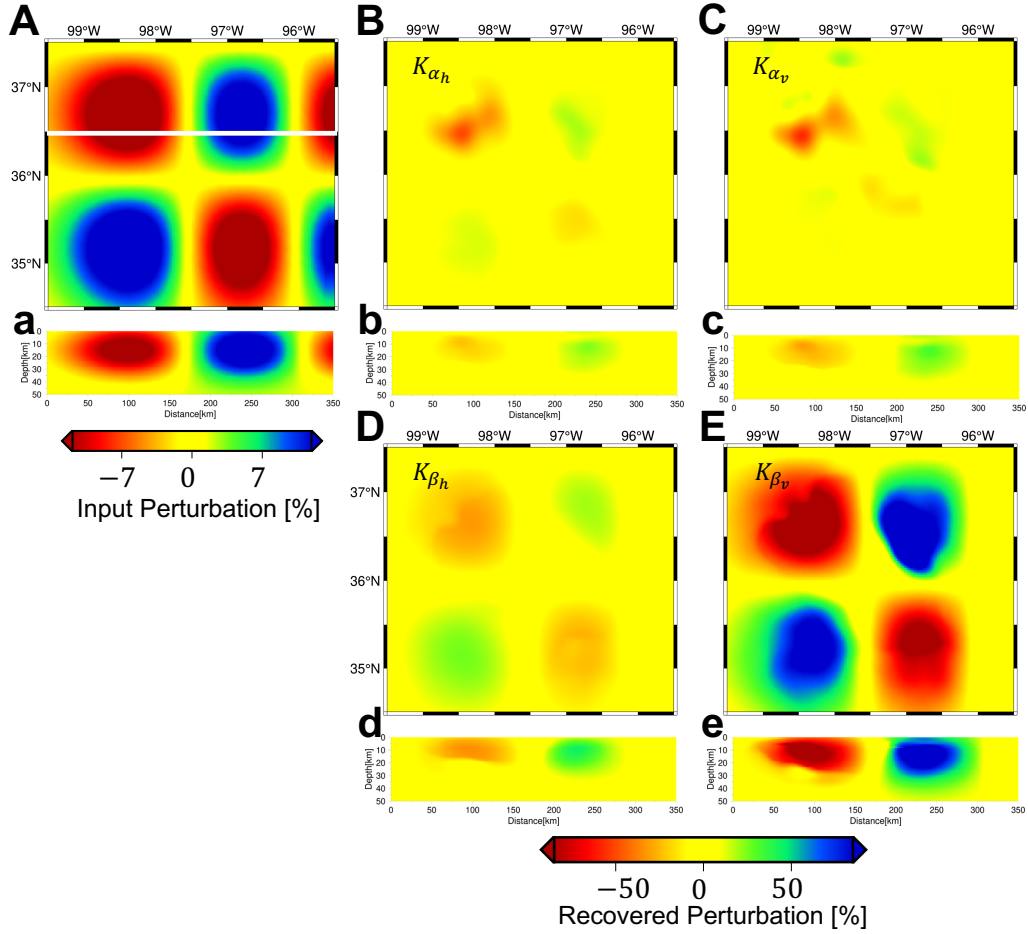


Figure 8. A checkerboard model and corresponding action of the Hessian on velocity perturbation. Panel A shows the distribution of Gaussian anomalies in the checkerboard model. Panels B, C, D and E are the action of the Hessian on 15% perturbations in α_h , α_v , β_h and β_v , respectively. Panels a, b, c, d and e are corresponding vertical sections of Panels A, B, C, D and E along latitude= $36.5^\circ N$ (white line in Panel A).

344 and shape-preferred orientation (SPO). When discussing the uppermost crust, the align-
345 ment of layered structures, pores and cracks could be alternative contributors of radial
346 anisotropy (Babuska & Cara, 1991; Shapiro et al., 2004; Lin et al., 2011).

347 In our inverted model, we observe positive radial anisotropy near the Earth’s sur-
348 face (Figures 5, and 6), which means that horizontally polarized shear waves V_{sh} are faster
349 than the vertically polarized components V_{sv} (Equation 3). The layered strata of sed-
350 imentary deposits might be the major cause of such positive radial anisotropy within the
351 uppermost crust (Crampin, 1989; Johnston & Christensen, 1995; Jiang & Denolle, 2022).
352 The comparatively deep positive anomalies around the Anadarko and Arkoma basins (Fig-
353 ure 6L) might correspond to their thick sedimentary strata, whereas the thin sedimen-
354 tary deposit in the Cherokee Shelf and Platform can be used to explain their shallow pos-
355 itive anomalies (Figures 6J and L). In addition, measured by laboratory experiments (Yan
356 et al., 2016), porosity and saturation of sandstone and shale might result in contrastive
357 radial anisotropy in basin and shelf areas as well.

358 In most cases, radial anisotropy within the middle crust is positive, due to the sub-
359 horizontal foliation plane of minerals in response to widespread horizontal-orientated tec-
360 tonic stress (Shapiro et al., 2004; Guo et al., 2012). However, a large negative volume
361 is observed in the middle crust of the inverted model (Figure 5 and 6). The negative ra-
362 dial anisotropy is often attributed to the injection of magma which forms vertical struc-
363 tures, like dikes (Mordret et al., 2015; Lynner et al., 2018). Nonetheless, few volcanic ac-
364 tivities are recorded in the geological history of Oklahoma. In the last decade, negative
365 radial anisotropy has also been reported in Tohoku and Kyushu (J. Wang & Zhao, 2013),
366 the Tehran basin (Shirzad & Shomali, 2014), the eastern Tibet (Huang et al., 2010), and
367 the Los Angeles basin (K. Wang et al., 2020), which potentially result from the preferred
368 orientation of mineral within the middle crust. Therefore, we also interpret the negative
369 volume in the inverted model as the response of anisotropic minerals. With respect to
370 the hexagonal symmetry of mica (Rey, 1993; Shapiro et al., 2004; G. E. Lloyd et al., 2009),
371 or orthorhombic symmetry of amphibole (Brownlee et al., 2017), negative radial anisotropy
372 can be caused by the sub-vertical foliation plane in minerals, which may suggest a po-
373 tentially vertical tectonic orientation at a local scale. Other than the fast axes in mica/amphibole
374 that are parallel to the direction of deformation, another possible candidate is plagio-
375 clase (Christensen, 1996; Almqvist & Mainprice, 2017; Bernard & Behr, 2017), which,
376 in laboratory measurements, exhibits strong anisotropy with fast axes aligning perpen-

377 dicular to the orientation of shear stresses (Shaocheng & David, 1988; Ji & Salisbury,
378 1993; Satsukawa et al., 2013). Based on the tectonic history in Oklahoma, the preferred
379 orientation of mica or plagioclase, representing different crystal structures, could be the
380 origin of negative radial anisotropy in the middle crust, but more investigations are needed
381 to distinguish detailed mechanisms.

382 **6.3 Depths of the Crystalline Basement**

383 Figure 9B shows the basement depth in Oklahoma obtained from borehole mea-
384 surements in the OGS database (<https://www.ou.edu/ogs>). A linear interpolation is
385 applied to smooth these point sampled results. The basement is shallow in the Chero-
386 kee Platform and the Southern Oklahoma Aulacogen (less than 0.5 km), and increases
387 in basin areas, such as around 5.0 km in the Arkoma Basin. These borehole measure-
388 ments are point samples and unevenly distributed, for instance, there are few measure-
389 ments in the Anadarko and Arkoma Basins, leading to poor constraints on the basement
390 depths in these areas.

391 Alternatively, we choose the $V_s=3.0$ km/s contour as a proxy to delineate the lat-
392 eral variations of the crystalline basement in Oklahoma (Durrheim & Mooney, 1991; Por-
393 ritt et al., 2020). The resulting map from our inverted 3-D velocity model has similar
394 spatial distribution as well-log measurements, for instance, shallow basement in the Chero-
395 kee Platform, the Cherokee Shelf, and the Southern Oklahoma Aulacogen, reflecting thin
396 unconsolidated sedimentary layers. Furthermore, in Figures 9C and D, we show crys-
397 talline basement maps extracted from other two 3-D velocity models: US2015 (Schmandt
398 et al., 2015) and US2016 (Shen & Ritzwoller, 2016). Model US2015 is estimated based
399 on multi-mode receiver functions and Rayleigh wave phase velocities (Schmandt et al.,
400 2015), while model US2016 is constrained by the joint inversion of ambient noise Rayleigh
401 wave dispersion curves and P-wave receiver functions (Shen & Ritzwoller, 2016). Their
402 spatial resolution is relatively low when focusing on Oklahoma, since both of them are
403 models for the entire United States. Similar to Figures 9A and B, we can find shallow
404 basements in the Cherokee Platform and the Southern Oklahoma Aulacogen in Figures 9C
405 and D. However, the Anadarko and the Arkoma Basins are not clear in Figures 9C and
406 D, and their depths are overall underestimated, such as around 3 to 4 km in contrast to
407 12 km from geological surveys and our new model.

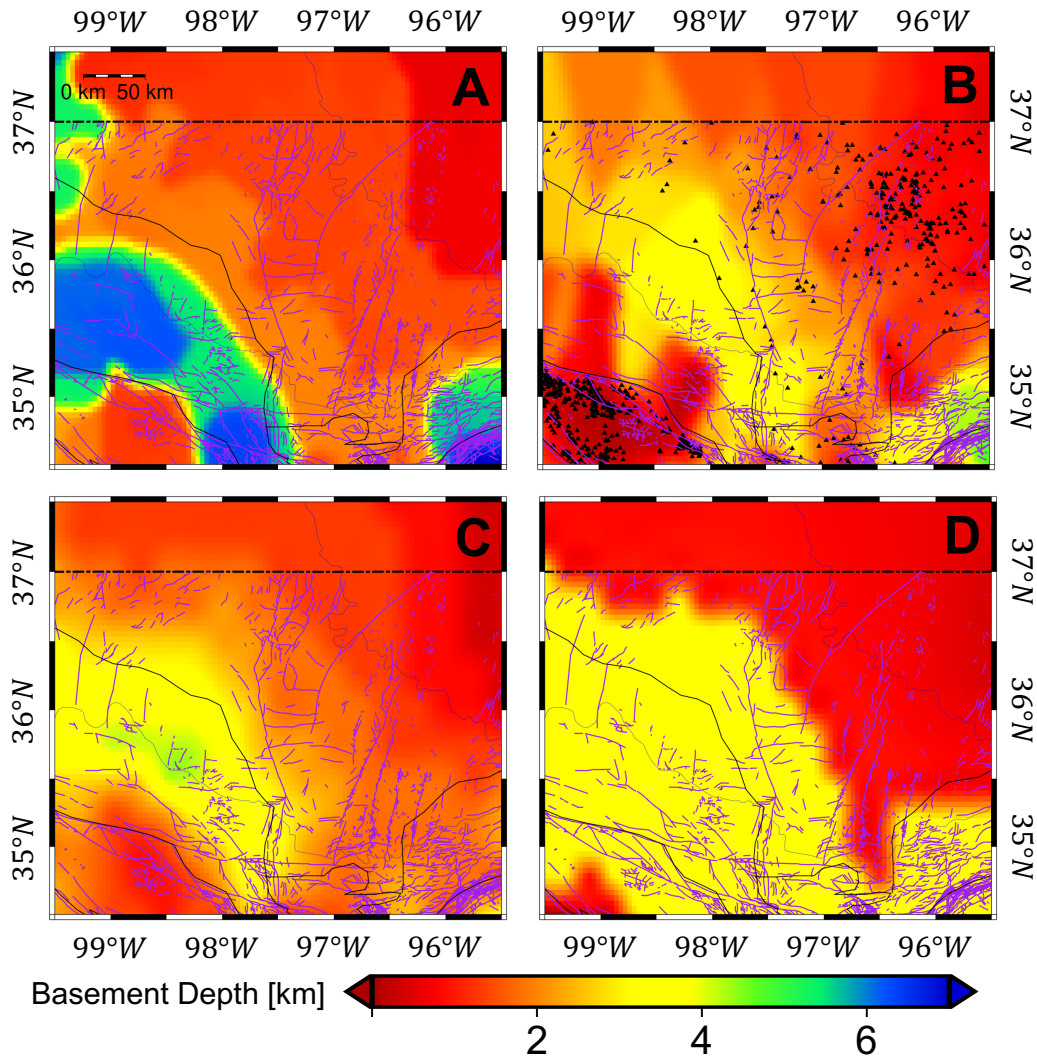


Figure 9. Comparison of crystalline basement depths extracted from our inverted 3D model (Panel A), well log measurements (Panel B), model US2016 from Shen and Ritzwoller (2016) (Panel C) and model US2015 from Schmandt et al. (2015) (Panel D). Black triangles in Panel B represent the locations of well logs (<https://www.ou.edu/ogs>).

6.4 Impact of 3-D velocity models on earthquake locations

To date, many studies have linked the increasing seismicity rate in Oklahoma to industry activities, such as saltwater injection (Keranen et al., 2013, 2014; Langenbruch & Zoback, 2016; X. Chen et al., 2018). Most existing earthquake catalogs are based on 1-D velocity profiles. They have played important roles to study the relation between industry activities and induced seismicity. Previous studies have demonstrated that lateral seismic velocity variations could bias the determination of centroid moment tensor solutions, as well as source locations (Q. Liu et al., 2004; X. Wang & Zhan, 2020). In this section, we illustrate the influence of lateral crustal velocity heterogeneities on earthquake locations in Oklahoma.

In Figure 10, 140 “synthetic earthquakes” are created and they are evenly distributed in the study region, with depths at 5, 10, 15 and 20 km. These “synthetic earthquakes” are relocated by using 58 stations in Oklahoma. Based on the inverted 3-D velocity model, the “observed travel-times” are calculated by using a fast marching method (Sethian, 1996; Sethian & Popovici, 1999), which are then inverted by using NonLinLoc (Lomax et al., 2000) to determine their locations. In the relocation, we use both inverted 3-D velocity model and the associated FWI-1D profile. As shown in Figures 10A and 11B, horizontal biases are overall negligible (less than 2 km) by taking lateral velocity variations or not. Whereas the depth errors are significant (Figures 10B, 10C and 11A). For instance, when using the 1-D velocity profile for earthquake relocation, the vertical errors can go as high as 10 km, which are reduced to around 2.5 km when we use the correct 3-D velocity model. Considering large uncertainties on the depths of relocated earthquakes, it is important to re-investigate the current catalogs by using the inverted 3-D velocity model, which allows us to better determine their depths and further investigate the triggering mechanisms of induced seismicity in Oklahoma.

7 Conclusion

With induced earthquakes and dense seismic stations deployed in Oklahoma, we construct a 3-D radially anisotropic crustal velocity model by using full waveform inversion. Our model can reduce the data misfit by around 40% for all three-component records. This 3-D model enables us to better delineate geological provinces in Oklahoma, such as the Anadarko Basin, the Cherokee Platform, and the Southern Oklahoma Aulacogen.

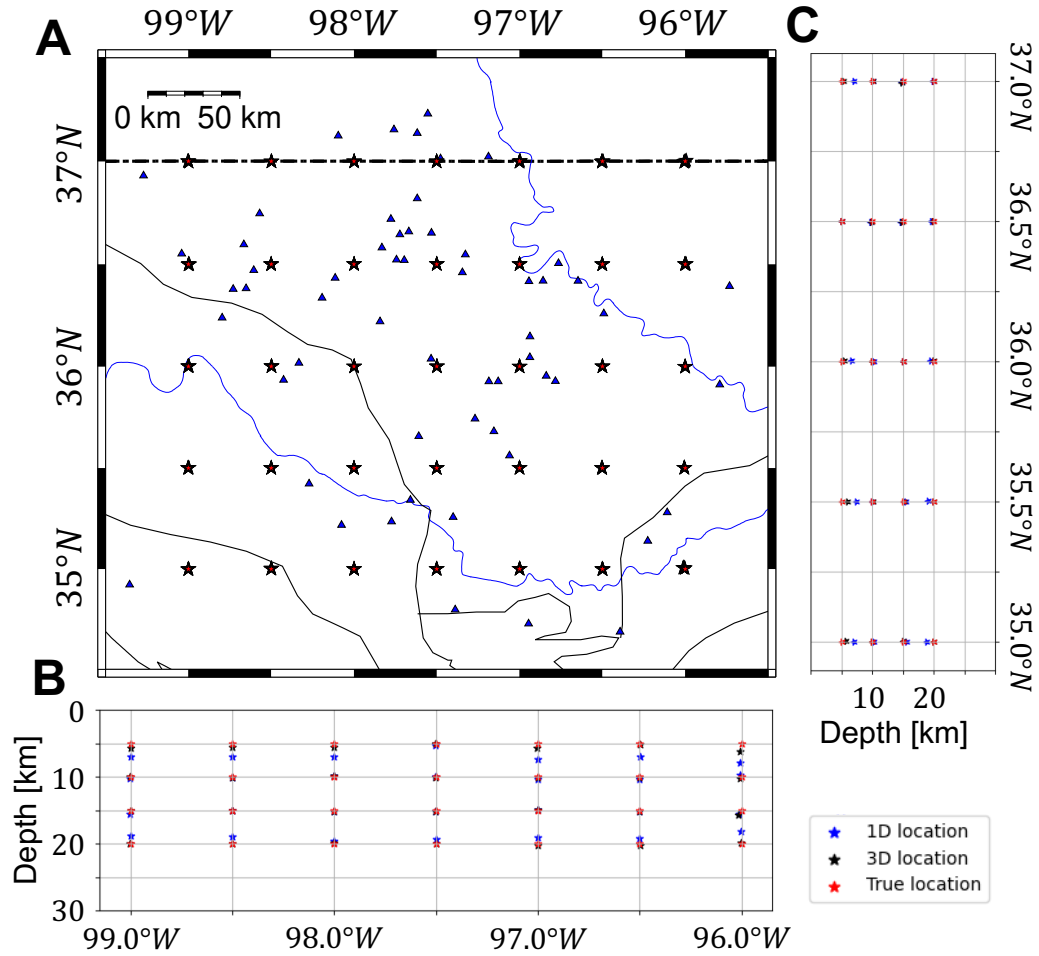


Figure 10. Comparison between earthquake locations based on 1-D (blue stars) and 3-D (black stars) velocity models by using synthetic earthquakes shown as red stars. Blue triangles in panel A denote 58 stations for the relocations. Panels B and C compare results along the vertical sections with latitude= $35.5^{\circ}N$ and longitude= $-98.5^{\circ}N$, respectively.

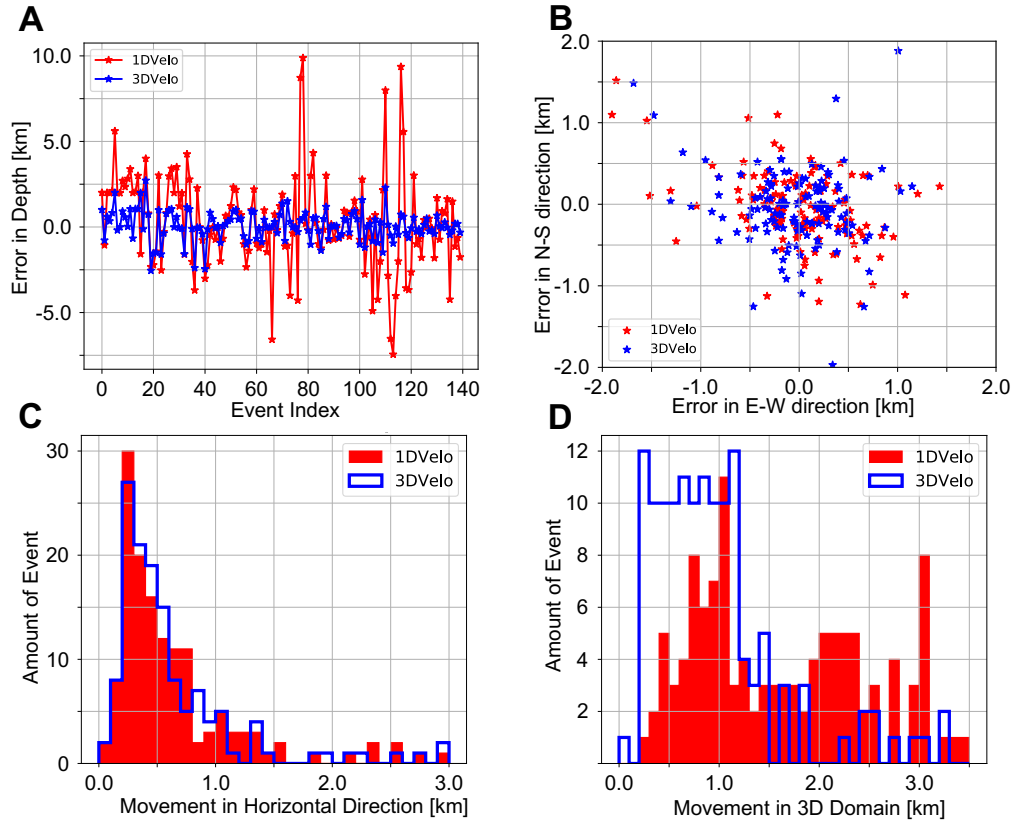


Figure 11. Impact of lateral seismic velocity variations on earthquake locations. Panels A and B illustrate vertical and horizontal errors from relocation based on 1-D (red) and 3-D (blue) velocity models. Panels C and D show the distribution of distances from the true location in the horizontal plane and 3-D volume.

439 Furthermore, we observe the upper crust is dominated by a thin layer with positive ra-
 440 dial anisotropy (+6%), while the middle to lower crust is characterized as relatively large
 441 negative radial anisotropy (-6%). These features might be related to deformation from
 442 background tectonic stress and preferential alignment of anisotropic minerals. We also
 443 extract the depths of the crystalline basement based on the inverted 3-D velocity model,
 444 which is overall consistent with borehole measurements. We further demonstrate that
 445 the 3-D velocity model allows us to improve the accuracy of earthquake locations, es-
 446 pecially for determining their depths. Therefore, the inverted 3-D velocity model pro-
 447 vides us an opportunity to better investigate induced earthquakes in Oklahoma.

448 Acknowledgments

449 This study is supported by NSF Grant EAR-*** and 3D+4D seismic inversion con-
 450 sortium at the University of Texas at Dallas. We thank the Texas Advanced Comput-
 451 ing Center for providing computational facilities for this study. Earthquake source pa-
 452 rameters, including time, location, and CMT solutions, are collected from the Earthquake
 453 Center of St. Louis University (<https://www.eas.slu.edu/eqc/eqc.html>). Raw seis-
 454 mic waveform records are downloaded from the Data Management Center of In corpo-
 455 rated Research Institutions for Seismology (<https://ds.iris.edu/ds/nodes/dmc/>). For-
 456 ward and adjoint wavefields are solved by using SPECFEM3D from Computational In-
 457 frastructure for Geodynamics (<https://github.com/SPECFEM/specfem3d>). Time win-
 458 dow selection is performed by using FLEXWIN ([https://github.com/geodynamics/](https://github.com/geodynamics/flexwin)
 459 [flexwin](https://github.com/geodynamics/flexwin)). Well-log information are collected from the Open Data Oklahoma Corpora-
 460 tion Commission (<https://www.ou.edu/ogs>). All figures are plotted by Generic Map-
 461 ping Tools (<https://www.generic-mapping-tools.org/>) and Obspy (<https://docs>
 462 [.obspy.org/](https://docs.obspy.org/)). This is UTD Geoscience contribution number ***.

463 References

- 464 Almquist, B. S., & Mainprice, D. (2017). Seismic properties and anisotropy of
 465 the continental crust: Predictions based on mineral texture and rock mi-
 466 crostructure. *Reviews of Geophysics*, *55*(2), 367–433. doi: doi.org/10.1002/
 467 2016RG000552
- 468 Amante, C., & Eakins, B. W. (2009). *ETOPO1 arc-minute global relief model:*
 469 *procedures, data sources and analysis* (Tech. Rep.). NOAA National Geophys-

- 470 ical Data Cente. Retrieved from <https://www.ngdc.noaa.gov/mgg/global/>
471 relief/ETOP01/docs/ETOP01.pdf
- 472 Anderson, D. L. (1961). Elastic wave propagation in layered anisotropic media.
473 *Journal of Geophysical Research*, 66(9), 2953–2963. doi: doi.org/10.1029/
474 JZ066i009p02953
- 475 Babuska, V., & Cara, M. (1991). *Seismic anisotropy in the Earth* (Vol. 10). Springer
476 Science & Business Media.
- 477 Ball, M. M., Henry, M. E., & Frezon, S. E. (1991). *Petroleum geology of the*
478 *Anadarko Basin region, province (115), Kansas, Oklahoma, and Texas* (Tech.
479 Rep.). doi: doi.org/10.3133/ofr88450W
- 480 Barbour, A. J., Norbeck, J. H., & Rubinstein, J. L. (2017). The effects of
481 varying injection rates in Osage County, Oklahoma, on the 2016 m w 5.8
482 Pawnee earthquake. *Seismological Research Letters*, 88(4), 1040–1053. doi:
483 doi.org/10.1785/0220170003
- 484 Beaty, K. S., Schmitt, D. R., & Sacchi, M. (2002). Simulated annealing inversion of
485 multimode Rayleigh wave dispersion curves for geological structure. *Geophys-*
486 *ical Journal International*, 151(2), 622–631. doi: doi.org/10.1046/j.1365-246X
487 .2002.01809.x
- 488 Bernard, R. E., & Behr, W. M. (2017). Fabric heterogeneity in the Mojave
489 lower crust and lithospheric mantle in Southern California. *Journal of Geo-*
490 *physical Research: Solid Earth*, 122(7), 5000–5025. doi: doi.org/10.1002/
491 2017JB014280
- 492 Bozdağ, E., Trampert, J., & Tromp, J. (2011). Misfit functions for full waveform in-
493 version based on instantaneous phase and envelope measurements. *Geophysical*
494 *Journal International*, 185(2), 845–870. doi: doi.org/10.1111/j.1365-246X.2011
495 .04970.x
- 496 Brownlee, S. J., Schulte-Pelkum, V., Raju, A., Mahan, K., Condit, C., & Orlandini,
497 O. F. (2017). Characteristics of deep crustal seismic anisotropy from a com-
498 pilation of rock elasticity tensors and their expression in receiver functions.
499 *Tectonics*, 36(9), 1835–1857. doi: doi.org/10.1002/2017TC004625
- 500 Bunks, C., Saleck, F. M., Zaleski, S., & Chavent, G. (1995). Multiscale seismic wave-
501 form inversion. *Geophysics*, 60(5), 1457–1473. doi: <https://doi.org/10.1190/1>
502 .1443880

- 503 Chen, G., Chen, J., Tape, C., Wu, H., & Tong, P. (2023). Double-difference
 504 adjoint tomography of the crust and uppermost mantle beneath Alaska.
 505 *Journal of Geophysical Research: Solid Earth*, *128*, e2022JB025168. doi:
 506 doi.org/10.1029/2022JB025168
- 507 Chen, M., Niu, F., Tromp, J., Lenardic, A., Lee, C.-T. A., Cao, W., & Ribeiro, J.
 508 (2017). Lithospheric foundering and underthrusting imaged beneath Tibet.
 509 *Nature communications*, *8*(1), 1–10. doi: doi.org/10.1038/ncomms15659
- 510 Chen, X., Haffener, J., Goebel, T. H., Meng, X., Peng, Z., & Chang, J. C. (2018).
 511 Temporal correlation between seismic moment and injection volume for an
 512 induced earthquake sequence in central Oklahoma. *Journal of Geophysical Re-*
 513 *search: Solid Earth*, *123*(4), 3047–3064. doi: doi.org/10.1002/2017JB014694
- 514 Chenoweth, P. A. (1968). Early Paleozoic (Arbuckle) overlap, southern
 515 mid-continent, United States. *AAPG Bulletin*, *52*(9), 1670–1688. doi:
 516 https://doi.org/10.1306/5D25C4C7-16C1-11D7-8645000102C1865D
- 517 Chow, B., Kaneko, Y., Tape, C., Modrak, R., & Townend, J. (2020). An automated
 518 workflow for adjoint tomography—waveform misfits and synthetic inversions
 519 for the North Island, New Zealand. *Geophysical Journal International*, *223*(3),
 520 1461–1480. doi: doi.org/10.1093/gji/ggaa381
- 521 Christensen, N. I. (1996). Poisson’s ratio and crustal seismology. *Journal of*
 522 *Geophysical Research: Solid Earth*, *101*(B2), 3139–3156. doi: doi.org/10.1029/
 523 95JB03446
- 524 Cramer, C. H., Bauer, R. A., Chung, J.-w., Rogers, J. D., Pierce, L., Voigt, V., ...
 525 others (2017). St. louis area earthquake hazards mapping project: Seismic and
 526 liquefaction hazard maps. *Seismological Research Letters*, *88*(1), 206–223.
- 527 Crampin, S. (1989). Suggestions for a consistent terminology for seismic anisotropy
 528 1. *Geophysical prospecting*, *37*(7), 753–770. doi: doi.org/10.1111/j.1365-2478
 529 .1989.tb02232.x
- 530 Dal Moro, G., Pipan, M., & Gabrielli, P. (2007). Rayleigh wave dispersion
 531 curve inversion via genetic algorithms and marginal posterior probabilit-
 532 ity density estimation. *Journal of Applied Geophysics*, *61*(1), 39–55. doi:
 533 doi.org/10.1016/j.jappgeo.2006.04.002
- 534 Darold, A. P., Holland, A. A., Morris, J. K., & Gibson, A. R. (2015). *Oklahoma*
 535 *earthquake summary report 2014* (Tech. Rep.). Okla. Geol. Surv. Open-

- 536 File Rept. OF1-2015. Retrieved from [http://ogs.ou.edu/docs/openfile/](http://ogs.ou.edu/docs/openfile/OF1-2015.pdf)
537 [OF1-2015.pdf](http://ogs.ou.edu/docs/openfile/OF1-2015.pdf)
- 538 Debayle, E., & Kennett, B. (2000). Anisotropy in the Australasian upper mantle
539 from Love and Rayleigh waveform inversion. *Earth and Planetary Science Letters*, *184*(1), 339–351. doi: [doi.org/10.1016/S0012-821X\(00\)00314-9](https://doi.org/10.1016/S0012-821X(00)00314-9)
540
- 541 Durrheim, R. J., & Mooney, W. D. (1991). Archean and Proterozoic crustal evolu-
542 tion: Evidence from crustal seismology. *Geology*, *19*(6), 606–609. doi: [doi.org/](https://doi.org/10.1130/0091-7613(1991)019(0606:AAPCEE)2.3.CO;2)
543 [10.1130/0091-7613\(1991\)019\(0606:AAPCEE\)2.3.CO;2](https://doi.org/10.1130/0091-7613(1991)019(0606:AAPCEE)2.3.CO;2)
- 544 Ellsworth, W. L. (2013). Injection-induced earthquakes. *Science*, *341*(6142). doi: [doi](https://doi.org/10.1126/science.1225942)
545 [.org/10.1126/science.1225942](https://doi.org/10.1126/science.1225942)
- 546 Evans, J. L. (1979). Major structural and stratigraphic features of the
547 Anadarko basin. , *61*, 2116. doi: [doi.org/10.1306/2F9188A1-16CE-11D7-](https://doi.org/10.1306/2F9188A1-16CE-11D7-8645000102C1865D)
548 [-8645000102C1865D](https://doi.org/10.1306/2F9188A1-16CE-11D7-8645000102C1865D)
- 549 Fichtner, A., Kennett, B. L., Igel, H., & Bunge, H.-P. (2009). Full seismic wave-
550 form tomography for upper-mantle structure in the Australasian region using
551 adjoint methods. *Geophysical Journal International*, *179*(3), 1703–1725. doi:
552 doi.org/10.1111/j.1365-246X.2009.04368.x
- 553 Fichtner, A., Trampert, J., Cupillard, P., Saygin, E., Taymaz, T., Capdeville, Y., &
554 Villasenor, A. (2013). Multiscale full waveform inversion. *Geophysical Journal*
555 *International*, *194*(1), 534–556. doi: doi.org/10.1093/gji/ggt118
- 556 Fletcher, R., & Reeves, C. M. (1964). Function minimization by conjugate gradients.
557 *The computer journal*, *7*(2), 149–154. doi: doi.org/10.1093/comjnl/7.2.149
- 558 Font, Y., Segovia, M., Vaca, S., & Theunissen, T. (2013). Seismicity patterns along
559 the Ecuadorian subduction zone: new constraints from earthquake location
560 in a 3-D a priori velocity model. *Geophysical Journal International*, *193*(1),
561 263–286. doi: doi.org/10.1093/gji/ggs083
- 562 Fouch, M. J., & Rondenay, S. (2006). Seismic anisotropy beneath stable continental
563 interiors. *Physics of the Earth and Planetary Interiors*, *158*(2-4), 292–320. doi:
564 doi.org/10.1016/j.pepi.2006.03.024
- 565 French, S., & Romanowicz, B. A. (2014). Whole-mantle radially anisotropic shear
566 velocity structure from spectral-element waveform tomography. *Geophysical*
567 *Journal International*, *199*(3), 1303–1327. doi: doi.org/10.1093/gji/ggu334
- 568 Guo, Z., Gao, X., Wang, W., & Yao, Z. (2012). Upper-and mid-crustal radial

- 569 anisotropy beneath the central Himalaya and southern Tibet from seismic am-
570 bient noise tomography. *Geophysical Journal International*, 189(2), 1169–1182.
571 doi: doi.org/10.1111/j.1365-246X.2012.05425.x
- 572 Hamilton, W. B. (1956). Precambrian rocks of Wichita and Arbuckle mountains,
573 Oklahoma. *Geological Society of America Bulletin*, 67(10), 1319–1330. doi: doi
574 .org/10.1130/0016-7606(1956)67[1319:PROWAA]2.0.CO;2
- 575 Harkrider, D. G. (1964). Surface waves in multilayered elastic media i. Rayleigh
576 and Love waves from buried sources in a multilayered elastic half-space. *Bul-
577 letin of the Seismological Society of America*, 54(2), 627–679. doi: doi.org/10
578 .1785/BSSA0540020627
- 579 Herrmann, R. B. (2013). Computer programs in seismology: An evolving tool for in-
580 struction and research. *Seismological Research Letters*, 84(6), 1081–1088. doi:
581 doi.org/10.1785/0220110096
- 582 Higley, D. K., Cook, T. A., & Pawlewicz, M. J. (2014). Petroleum systems and
583 assessment of undiscovered oil and gas in the Anadarko Basin Province, Col-
584 orado, Kansas, Oklahoma, and Texas—Woodford Shale assessment units. , 58.
585 doi: doi.org/10.3133/ds69EE
- 586 Holland, A. A. (2013a). Earthquakes triggered by hydraulic fracturing in south-
587 central Oklahoma. *Bulletin of the Seismological Society of America*, 103(3),
588 1784–1792. doi: doi.org/10.1785/0120120109
- 589 Holland, A. A. (2013b). Optimal fault orientations within oklahoma. *Seismological
590 Research Letters*, 84(5), 876–890. doi: doi.org/10.1785/0220120153
- 591 Houtz, R. E., & Ludwig, W. J. (1979). Distribution of reverberant subbottom layers
592 in the southwest Pacific basin. *Journal of Geophysical Research: Solid Earth*,
593 84(B7), 3497–3504. doi: doi.org/10.1029/JB084iB07p03497
- 594 Huang, H., Yao, H., & van der Hilst, R. D. (2010). Radial anisotropy in the crust
595 of SE Tibet and SW China from ambient noise interferometry. *Geophysical Re-
596 search Letters*, 37(21). doi: doi.org/10.1029/2010GL044981
- 597 Ji, S., & Salisbury, M. H. (1993). Shear-wave velocities, anisotropy and splitting
598 in high-grade mylonites. *Tectonophysics*, 221(3-4), 453–473. doi: doi.org/10
599 .1016/0040-1951(93)90173-H
- 600 Jiang, C., & Denolle, M. A. (2022). Pronounced Seismic Anisotropy in Kanto Sedi-
601 mentary Basin: A Case Study of Using Dense Arrays, Ambient Noise Seismol-

- 602 ogy, and Multi-Modal Surface-Wave Imaging. *Journal of Geophysical Research:*
603 *Solid Earth*, 127(8), e2022JB024613. doi: doi.org/10.1029/2022JB024613
- 604 Johnson, K. S. (1996). *Geology of Oklahoma* (Tech. Rep.). Oklahoma Geologi-
605 cal Survey. Retrieved from [http://ogs.ou.edu/docs/specialpublications/](http://ogs.ou.edu/docs/specialpublications/SP96-5.pdf)
606 [SP96-5.pdf](http://ogs.ou.edu/docs/specialpublications/SP96-5.pdf)
- 607 Johnson, K. S., & Luza, K. V. (2008). *Earth sciences and mineral resources of Okla-*
608 *homa* (Tech. Rep.). Oklahoma Geological Survey. Retrieved from [http://www](http://www.ogs.ou.edu/pubsscanned/EP9_A11.pdf)
609 [.ogs.ou.edu/pubsscanned/EP9_A11.pdf](http://www.ogs.ou.edu/pubsscanned/EP9_A11.pdf)
- 610 Johnston, J. E., & Christensen, N. I. (1995). Seismic anisotropy of shales. *Journal of*
611 *Geophysical Research: Solid Earth*, 100(B4), 5991–6003. doi: doi.org/10.1029/
612 95JB00031
- 613 Keller, G. R. (2013). The Moho of North America: A brief review focused on recent
614 studies. *Tectonophysics*, 609, 45–55. doi: doi.org/10.1016/j.tecto.2013.07.031
- 615 Keranen, K. M., Savage, H. M., Abers, G. A., & Cochran, E. S. (2013). Potentially
616 induced earthquakes in Oklahoma, USA: Links between wastewater injection
617 and the 2011 Mw 5.7 earthquake sequence. *Geology*, 41(6), 699–702. doi:
618 doi.org/10.1130/G34045.1
- 619 Keranen, K. M., Weingarten, M., Abers, G. A., Bekins, B. A., & Ge, S. (2014).
620 Sharp increase in central Oklahoma seismicity since 2008 induced by massive
621 wastewater injection. *Science*, 345(6195), 448–451. doi: doi.org/10.1126/
622 science.1255802
- 623 Kolawole, F., Turko, M. S., & Carpenter, B. M. (2020). Basement-controlled defor-
624 mation of sedimentary sequences, Anadarko Shelf, Oklahoma. *Basin Research*,
625 32(6), 1365–1387. doi: <https://doi.org/10.1111/bre.12433>
- 626 Komatitsch, D., & Tromp, J. (1999). Introduction to the spectral element method
627 for three-dimensional seismic wave propagation. *Geophysical journal interna-*
628 *tional*, 139(3), 806–822. doi: doi.org/10.1046/j.1365-246x.1999.00967.x
- 629 Lailly, P., & Bednar, J. (1983). The seismic inverse problem as a sequence of be-
630 fore stack migrations. In *Conference on inverse scattering: theory and applica-*
631 *tion* (pp. 206–220).
- 632 Langenbruch, C., & Zoback, M. D. (2016). How will induced seismicity in Okla-
633 homa respond to decreased saltwater injection rates? *Science advances*, 2(11),
634 e1601542. doi: <https://doi.org/10.1126/sciadv.1601542>

- 635 Lei, W., Ruan, Y., Bozdağ, E., Peter, D., Lefebvre, M., Komatitsch, D., . . . Pug-
636 mire, D. (2020). Global adjoint tomography—model GLAD-M25. *Geophys-*
637 *ical Journal International*, *223*(1), 1–21. doi: [https://doi.org/10.1093/gji/](https://doi.org/10.1093/gji/ggaa253)
638 [ggaa253](https://doi.org/10.1093/gji/ggaa253)
- 639 Lin, F.-C., Ritzwoller, M. H., Yang, Y., Moschetti, M. P., & Fouch, M. J. (2011).
640 Complex and variable crustal and uppermost mantle seismic anisotropy
641 in the western United States. *Nature Geoscience*, *4*(1), 55–61. doi:
642 <https://doi.org/10.1038/ngeo1036>
- 643 Liu, Q., Polet, J., Komatitsch, D., & Tromp, J. (2004). Spectral-element moment
644 tensor inversions for earthquakes in southern California. *Bulletin of the Seis-*
645 *mological Society of America*, *94*(5), 1748–1761. doi: [https://doi.org/10.1785/](https://doi.org/10.1785/012004038)
646 [012004038](https://doi.org/10.1785/012004038)
- 647 Liu, Y., Teng, J., Xu, T., Wang, Y., Liu, Q., & Badal, J. (2017). Robust time-
648 domain full waveform inversion with normalized zero-lag cross-correlation
649 objective function. *Geophysical Journal International*, *209*(1), 106–122. doi:
650 <https://doi.org/10.1093/gji/ggw485>
- 651 Lloyd, A., Wiens, D., Zhu, H., Tromp, J., Nyblade, A., Aster, R., . . . others (2020).
652 Seismic structure of the Antarctic upper mantle imaged with adjoint to-
653 mography. *Journal of Geophysical Research: Solid Earth*, *125*(3). doi:
654 <https://doi.org/10.1029/2019JB017823>
- 655 Lloyd, G. E., Butler, R. W., Casey, M., & Mainprice, D. (2009). Mica, deformation
656 fabrics and the seismic properties of the continental crust. *Earth and Planetary*
657 *Science Letters*, *288*(1-2), 320–328. doi: <https://doi.org/10.1016/j.epsl.2009.09>
658 [.035](https://doi.org/10.1016/j.epsl.2009.09)
- 659 Lomax, A., Virieux, J., Volant, P., & Berge-Thierry, C. (2000). Probabilistic earth-
660 quake location in 3D and layered models. In *Advances in seismic event location*
661 (pp. 101–134). Springer. doi: [10.1007/978-94-015-9536-0_5](https://doi.org/10.1007/978-94-015-9536-0_5)
- 662 Long, M. D. (2013). Constraints on subduction geodynamics from seismic
663 anisotropy. *Reviews of Geophysics*, *51*(1), 76–112. doi: [https://doi.org/](https://doi.org/10.1002/rog.20008)
664 [10.1002/rog.20008](https://doi.org/10.1002/rog.20008)
- 665 Lund Snee, J.-E., & Zoback, M. D. (2020). Multiscale variations of the crustal stress
666 field throughout North America. *Nature Communications*, *11*(1), 1951. doi:
667 <https://doi.org/10.1038/s41467-020-15841-5>

- 668 Luo, Y. (2012). *Seismic imaging and inversion based on spectral-element and ad-*
 669 *joint methods* (Doctoral dissertation, Princeton University). Retrieved from
 670 <https://dataspace.princeton.edu/handle/88435/dsp018623hx78j>
- 671 Luo, Y., Modrak, R., & Tromp, J. (2015). Strategies in adjoint tomography. In
 672 *Handbook of Geomathematics: Second Edition* (pp. 1943–2001). Springer
 673 Berlin Heidelberg. doi: 10.1007/978-3-642-54551-1_96
- 674 Luo, Y., & Schuster, G. T. (1991). Wave-equation travelttime inversion. *Geophysics*,
 675 *56*(5), 645–653. doi: <https://doi.org/10.1190/1.1443081>
- 676 Lynner, C., Beck, S. L., Zandt, G., Porritt, R. W., Lin, F.-C., & Eilon, Z. C.
 677 (2018). Midcrustal deformation in the Central Andes constrained by radial
 678 anisotropy. *Journal of Geophysical Research: Solid Earth*, *123*(6), 4798–4813.
 679 doi: <https://doi.org/10.1029/2017JB014936>
- 680 Ma, Y., & Hale, D. (2013). Wave-equation reflection travelttime inversion with dy-
 681 namic warping and full-waveform inversion. *Geophysics*, *78*(6), R223–R233.
 682 doi: <https://doi.org/10.1190/geo2013-0004.1>
- 683 Maggi, A., Tape, C., Chen, M., Chao, D., & Tromp, J. (2009). An automated time-
 684 window selection algorithm for seismic tomography. *Geophysical Journal In-*
 685 *ternational*, *178*(1), 257–281. doi: <https://doi.org/10.1111/j.1365-246X.2009>
 686 [.04099.x](https://doi.org/10.1111/j.1365-246X.2009.04099.x)
- 687 Marsh, S., & Holland, A. (2016). *Comprehensive fault database and interpretive fault*
 688 *map of Oklahoma* (Tech. Rep.). Oklahoma Geological Survey. Retrieved from
 689 <http://ogs.ou.edu/docs/openfile/OF2-2016.pdf>
- 690 Matthies, H., & Strang, G. (1979). The solution of nonlinear finite element equa-
 691 tions. *International journal for numerical methods in engineering*, *14*(11),
 692 1613–1626. doi: <https://doi.org/10.1002/nme.1620141104>
- 693 McNamara, D. E., Benz, H. M., Herrmann, R. B., Bergman, E. A., Earle, P., Hol-
 694 land, A., . . . Gassner, A. (2015). Earthquake hypocenters and focal mecha-
 695 nisms in central Oklahoma reveal a complex system of reactivated subsurface
 696 strike-slip faulting. *Geophysical Research Letters*, *42*(8), 2742–2749. doi:
 697 <https://doi.org/10.1002/2014GL062730>
- 698 Métivier, L., Brossier, R., Méridot, Q., Oudet, E., & Virieux, J. (2016). Mea-
 699 suring the misfit between seismograms using an optimal transport distance:
 700 Application to full waveform inversion. *Geophysical Supplements to the*

- 701 *Monthly Notices of the Royal Astronomical Society*, 205(1), 345–377. doi:
702 doi.org/10.1093/gji/ggw014
- 703 Michellini, A., & Lomax, A. (2004). The effect of velocity structure errors on double-
704 difference earthquake location. *Geophysical Research Letters*, 31(9). doi:
705 https://doi.org/10.1093/gji/ggw014
- 706 Mitchell, B., & Landisman, M. (1970). Interpretation of a crustal section across
707 Oklahoma. *Geological Society of America Bulletin*, 81(9), 2647–2656. doi:
708 https://doi.org/10.1130/0016-7606(1970)81[2647:IOACSA]2.0.CO;2
- 709 Mordret, A., Rivet, D., Landès, M., & Shapiro, N. M. (2015). Three-dimensional
710 shear velocity anisotropic model of Piton de la Fournaise Volcano (La Réunion
711 Island) from ambient seismic noise. *Journal of Geophysical Research: Solid
712 Earth*, 120(1), 406–427. doi: https://doi.org/10.1002/2014JB011654
- 713 Mueller, C. S. (2019). Earthquake catalogs for the USGS national seismic hazard
714 maps. *Seismological Research Letters*, 90(1), 251–261. doi: https://doi.org/10
715 .1785/0220170108
- 716 Northcutt, R. A., & Campbell, J. A. (1996). Geologic provinces of Oklahoma. *The
717 Shale Shaker*, 46(5), 99–103. doi: 10.1007/978-94-011-5098-9_2
- 718 Pennington, C., & Chen, X. (2017). Coulomb stress interactions during the M w
719 5.8 Pawnee sequence. *Seismological Research Letters*, 88(4), 1024–1031. doi:
720 https://doi.org/10.1785/0220170011
- 721 Perry, W. J. (1989). *Tectonic evolution of the Anadarko Basin region, Oklahoma*
722 (No. 1866). Department of the Interior, US Geological Survey. doi: https://doi
723 .org/10.3133/b1866A
- 724 Peter, D., Komatitsch, D., Luo, Y., Martin, R., Le Goff, N., Casarotti, E., . . . others
725 (2011). Forward and adjoint simulations of seismic wave propagation on fully
726 unstructured hexahedral meshes. *Geophysical Journal International*, 186(2),
727 721–739. doi: doi.org/10.1111/j.1365-246X.2011.05044.x
- 728 Porritt, R., Savvaidis, A., Young, B., Shirley, M., & Li, P. (2020). Crustal Structure
729 in Southeastern Texas From Joint Inversion of Ambient Seismic Noise and
730 P to S Receiver Functions. *Geochemistry, Geophysics, Geosystems*, 21(7),
731 e2019GC008866. doi: https://doi.org/10.1029/2019GC008866
- 732 Rey, P. (1993). Seismic and tectono-metamorphic characters of the lower continental
733 crust in Phanerozoic areas: A consequence of post-thickening extension. *Tec-*

- 734 *tonics*, 12(2), 580–590. doi: <https://doi.org/10.1029/92TC01568>
- 735 Rickers, F., Fichtner, A., & Trampert, J. (2013). The Iceland–Jan Mayen plume sys-
736 tem and its impact on mantle dynamics in the North Atlantic region: evidence
737 from full-waveform inversion. *Earth and Planetary Science Letters*, 367, 39–51.
738 doi: <https://doi.org/10.1016/j.epsl.2013.02.022>
- 739 Rubinstein, J. L., & Mahani, A. B. (2015). Myths and facts on wastewater injection,
740 hydraulic fracturing, enhanced oil recovery, and induced seismicity. *Seismo-
741 logical Research Letters*, 86(4), 1060–1067. doi: [https://doi.org/10.1785/
742 0220150067](https://doi.org/10.1785/0220150067)
- 743 Sams, M., Neep, J., Worthington, M., & King, M. (1997). The measurement of ve-
744 locity dispersion and frequency-dependent intrinsic attenuation in sedimentary
745 rocks. *Geophysics*, 62(5), 1456–1464. doi: <https://doi.org/10.1190/1.1444249>
- 746 Satsukawa, T., Ildfonse, B., Mainprice, D., Morales, L., Michibayashi, K., & Barou,
747 F. (2013). A database of plagioclase crystal preferred orientations (CPO)
748 and microstructures—implications for CPO origin, strength, symmetry and
749 seismic anisotropy in gabbroic rocks. *Solid Earth*, 4(2), 511–542. doi:
750 <https://doi.org/10.5194/se-4-511-2013>
- 751 Schmandt, B., Lin, F.-C., & Karlstrom, K. E. (2015). Distinct crustal isostasy
752 trends east and west of the Rocky Mountain Front. *Geophysical Research
753 Letters*, 42(23), 10–290. doi: <https://doi.org/10.1002/2015GL066593>
- 754 Schoenball, M., & Ellsworth, W. L. (2017). Waveform-relocated earthquake cat-
755 alog for Oklahoma and southern Kansas illuminates the regional fault net-
756 work. *Seismological Research Letters*, 88(5), 1252–1258. doi: [https://doi.org/
757 10.1785/0220170083](https://doi.org/10.1785/0220170083)
- 758 Sethian, J. A. (1996). A fast marching level set method for monotonically advanc-
759 ing fronts. *Proceedings of the National Academy of Sciences*, 93(4), 1591–1595.
760 doi: <https://doi.org/10.1073/pnas.93.4.1591>
- 761 Sethian, J. A., & Popovici, A. M. (1999). 3-D travelttime computation using the fast
762 marching method. *Geophysics*, 64(2), 516–523. doi: [https://doi.org/10.1190/1
763 .1444558](https://doi.org/10.1190/1.1444558)
- 764 Shaocheng, J., & David, M. (1988). Natural deformation fabrics of plagioclase:
765 implications for slip systems and seismic anisotropy. *Tectonophysics*, 147(1-2),
766 145–163. doi: [https://doi.org/10.1016/0040-1951\(88\)90153-9](https://doi.org/10.1016/0040-1951(88)90153-9)

- 767 Shapiro, N. M., Ritzwoller, M. H., Molnar, P., & Levin, V. (2004). Thinning and
 768 flow of Tibetan crust constrained by seismic anisotropy. *Science*, *305*(5681),
 769 233–236. doi: <https://doi.org/10.1126/science.1098276>
- 770 Shen, W., & Ritzwoller, M. H. (2016). Crustal and uppermost mantle structure
 771 beneath the United States. *Journal of Geophysical Research: Solid Earth*,
 772 *121*(6), 4306–4342. doi: <https://doi.org/10.1002/2016JB012887>
- 773 Shirzad, T., & Shomali, Z. H. (2014). Shallow crustal radial anisotropy beneath
 774 the Tehran basin of Iran from seismic ambient noise tomography. *Physics of*
 775 *the Earth and Planetary Interiors*, *231*, 16–29. doi: [https://doi.org/10.1016/j](https://doi.org/10.1016/j.pepi.2014.04.001)
 776 [.pepi.2014.04.001](https://doi.org/10.1016/j.pepi.2014.04.001)
- 777 Skoumal, R. J., Ries, R., Brudzinski, M. R., Barbour, A. J., & Currie, B. S.
 778 (2018). Earthquakes induced by hydraulic fracturing are pervasive in Okla-
 779 homa. *Journal of Geophysical Research: Solid Earth*, *123*(12), 10–918. doi:
 780 doi.org/10.1029/2018JB016790
- 781 Sloss, L. L. (1988). *Sedimentary Cover—North American Craton: US*. Geological
 782 Society of America.
- 783 Sumy, D. F., Cochran, E. S., Keranen, K. M., Wei, M., & Abers, G. A. (2014).
 784 Observations of static Coulomb stress triggering of the November 2011 M5.7
 785 Oklahoma earthquake sequence. *Journal of Geophysical Research: Solid Earth*,
 786 *119*(3), 1904–1923. doi: <https://doi.org/10.1002/2013JB010612>
- 787 Takemura, S., Yoshimoto, K., & Shiomi, K. (2021). Long-period ground motion
 788 simulation using centroid moment tensor inversion solutions based on the re-
 789 gional three-dimensional model in the Kanto region, Japan. *Earth, Planets and*
 790 *Space*, *73*(1), 1–18. doi: <https://doi.org/10.1186/s40623-020-01348-2>
- 791 Tan, J., Langston, C. A., & Ni, S. (2021). Shallow shear-wave velocity structure in
 792 Oklahoma based on the joint inversion of ambient noise dispersion and tele-
 793 seismic P-wave receiver functions. *Bulletin of the Seismological Society of*
 794 *America*, *111*(2), 654–670. doi: <https://doi.org/10.1785/0120200246>
- 795 Tao, K., Grand, S. P., & Niu, F. (2017). Full-waveform inversion of triplicated
 796 data using a normalized-correlation-coefficient-based misfit function. *Geophysi-*
 797 *cal Journal International*, *210*(3), 1517–1524. doi: [https://doi.org/10.1093/gji/](https://doi.org/10.1093/gji/ggx249)
 798 [ggx249](https://doi.org/10.1093/gji/ggx249)
- 799 Tao, K., Grand, S. P., & Niu, F. (2018). Seismic structure of the upper mantle

- 800 beneath eastern Asia from full waveform seismic tomography. *Geochemistry,*
 801 *Geophysics, Geosystems*, 19(8), 2732–2763. doi: [https://doi.org/10.1029/](https://doi.org/10.1029/2018GC007460)
 802 2018GC007460
- 803 Tape, C., Liu, Q., Maggi, A., & Tromp, J. (2010). Seismic tomography of the south-
 804 ern California crust based on spectral-element and adjoint methods. *Geophysical*
 805 *Journal International*, 180(1), 433–462. doi: [https://doi.org/10.1111/j.1365-](https://doi.org/10.1111/j.1365-246X.2009.04429.x)
 806 -246X.2009.04429.x
- 807 Tape, C., Liu, Q., & Tromp, J. (2007). Finite-frequency tomography us-
 808 ing adjoint methods—Methodology and examples using membrane sur-
 809 face waves. *Geophysical Journal International*, 168(3), 1105–1129. doi:
 810 <https://doi.org/10.1111/j.1365-246X.2006.03191.x>
- 811 Tarantola, A. (1984). Inversion of seismic reflection data in the acoustic approxima-
 812 tion. *Geophysics*, 49(8), 1259–1266. doi: <https://doi.org/10.1190/1.1441754>
- 813 Thurber, C. H. (1983). Earthquake locations and three-dimensional crustal struc-
 814 ture in the Coyote Lake area, central California. *Journal of Geophysical*
 815 *Research: Solid Earth*, 88(B10), 8226–8236. doi: [https://doi.org/10.1029/](https://doi.org/10.1029/JB088iB10p08226)
 816 JB088iB10p08226
- 817 Tromp, J., Tape, C., & Liu, Q. (2005). Seismic tomography, adjoint methods, time
 818 reversal and banana-doughnut kernels. *Geophysical Journal International*,
 819 160(1), 195–216. doi: <https://doi.org/10.1111/j.1365-246X.2004.02453.x>
- 820 Virieux, J., & Operto, S. (2009). An overview of full-waveform inversion in explo-
 821 ration geophysics. *Geophysics*, 74(6), WCC1–WCC26. doi: [https://doi.org/10](https://doi.org/10.1190/1.3238367)
 822 .1190/1.3238367
- 823 Walsh, F. R., & Zoback, M. D. (2015). Oklahoma’s recent earthquakes and saltwa-
 824 ter disposal. *Science advances*, 1(5), e1500195. doi: [https://doi.org/10.1126/](https://doi.org/10.1126/sciadv.1500195)
 825 sciadv.1500195
- 826 Walter, J. I., Ogwari, P., Thiel, A., Ferrer, F., Woelfel, I., Chang, J. C., . . . Hol-
 827 land, A. A. (2020). The Oklahoma Geological Survey Statewide Seis-
 828 mic Network. *Seismological Research Letters*, 91(2A), 611–621. doi:
 829 <https://doi.org/10.1785/0220190211>
- 830 Wang, J., & Zhao, D. (2009). P-wave anisotropic tomography of the crust and up-
 831 per mantle under Hokkaido, Japan. *Tectonophysics*, 469(1-4), 137–149. doi:
 832 <https://doi.org/10.1016/j.tecto.2009.02.005>

- 833 Wang, J., & Zhao, D. (2013). P-wave tomography for 3-D radial and azimuthal
 834 anisotropy of Tohoku and Kyushu subduction zones. *Geophysical Journal In-*
 835 *ternational*, *193*(3), 1166–1181. doi: <https://doi.org/10.1093/gji/ggt086>
- 836 Wang, K., Jiang, C., Yang, Y., Schulte-Pelkum, V., & Liu, Q. (2020). Crustal
 837 deformation in Southern California constrained by radial anisotropy from
 838 ambient noise adjoint tomography. *Geophysical Research Letters*, *47*(12),
 839 e2020GL088580. doi: <https://doi.org/10.1029/2020GL088580>
- 840 Wang, X., & Zhan, Z. (2020). Moving from 1-D to 3-D velocity model: auto-
 841 mated waveform-based earthquake moment tensor inversion in the Los An-
 842 geles region. *Geophysical Journal International*, *220*(1), 218–234. doi:
 843 <https://doi.org/10.1093/gji/ggz435>
- 844 Warner, M., & Guasch, L. (2016). Adaptive waveform inversion: Theory. *Geo-*
 845 *physics*, *81*(6), R429–R445. doi: <https://doi.org/10.1190/geo2015-0387.1>
- 846 Whitaker, A. E., & Engelder, T. (2006). Plate-scale stress fields driving the tectonic
 847 evolution of the central Ouachita salient, Oklahoma and Arkansas. *Geological*
 848 *Society of America Bulletin*, *118*(5-6), 710–723. doi: [https://doi.org/10.1130/](https://doi.org/10.1130/B25780.1)
 849 [B25780.1](https://doi.org/10.1130/B25780.1)
- 850 Wu, R.-S., Luo, J., & Wu, B. (2014). Seismic envelope inversion and modulation
 851 signal model. *Geophysics*, *79*(3), WA13–WA24. doi: [https://doi.org/10.1190/](https://doi.org/10.1190/geo2013-0294.1)
 852 [geo2013-0294.1](https://doi.org/10.1190/geo2013-0294.1)
- 853 Xu, C., Cronin, T. P., McGinness, T. E., & Steer, B. (2009). Middle Atokan sed-
 854 iment gravity flows in the Red Oak field, Arkoma Basin, Oklahoma: A sed-
 855 imentary analysis using electrical borehole images and wireline logs. *AAPG*
 856 *bulletin*, *93*(1), 1–29. doi: <https://doi.org/10.1306/09030808054>
- 857 Yan, F., Han, D.-H., Sil, S., & Chen, X.-L. (2016). Analysis of seismic anisotropy
 858 parameters for sedimentary strata. *Geophysics*, *81*(5), D495–D502. doi:
 859 <https://doi.org/10.1190/geo2016-0062.1>
- 860 Yang, Y., & Engquist, B. (2018). Analysis of optimal transport and related misfit
 861 functions in full-waveform inversion. *Geophysics*, *83*(1), A7–A12. doi: [https://](https://doi.org/10.1190/geo2017-0264.1)
 862 doi.org/10.1190/geo2017-0264.1
- 863 Yu, Y., Song, J., Liu, K. H., & Gao, S. S. (2015). Determining crustal structure be-
 864 neath seismic stations overlying a low-velocity sedimentary layer using receiver
 865 functions. *Journal of Geophysical Research: Solid Earth*, *120*(5), 3208–3218.

- 866 doi: <https://doi.org/10.1002/2014JB011610>
- 867 Zhang, C., Yao, H., Liu, Q., Zhang, P., Yuan, Y. O., Feng, J., & Fang, L. (2018).
 868 Linear array ambient noise adjoint tomography reveals intense crust-mantle
 869 interactions in North China Craton. *Journal of Geophysical Research: Solid*
 870 *Earth*, *123*(1), 368–383. doi: <https://doi.org/10.1002/2017JB015019>
- 871 Zhu, H. (2018). Crustal wave speed structure of North Texas and Oklahoma based
 872 on ambient noise cross-correlation functions and adjoint tomography. *Geophys-*
 873 *ical Journal International*, *214*(1), 716–730. doi: [https://doi.org/10.1093/gji/](https://doi.org/10.1093/gji/ggy169)
 874 [ggy169](https://doi.org/10.1093/gji/ggy169)
- 875 Zhu, H., Bozdağ, E., & Tromp, J. (2015). Seismic structure of the European up-
 876 per mantle based on adjoint tomography. *Geophysical Journal International*,
 877 *201*(1), 18–52. doi: <https://doi.org/10.1093/gji/ggu492>
- 878 Zhu, H., & Fomel, S. (2016). Building good starting models for full-waveform inver-
 879 sion using adaptive matching filtering misfit. *Geophysics*, *81*(5), U61–U72. doi:
 880 <https://doi.org/10.1190/geo2015-0596.1>
- 881 Zhu, H., Komatitsch, D., & Tromp, J. (2017). Radial anisotropy of the North Amer-
 882 ican upper mantle based on adjoint tomography with USArray. *Geophysical*
 883 *Journal International*, *211*(1), 349–377. doi: [https://doi.org/10.1093/gji/](https://doi.org/10.1093/gji/ggx305)
 884 [ggx305](https://doi.org/10.1093/gji/ggx305)